

# UC San Diego

## UC San Diego Previously Published Works

### Title

Phase separation of ligand-activated enhancers licenses cooperative chromosomal enhancer assembly

### Permalink

<https://escholarship.org/uc/item/5c99q6c6>

### Journal

Nature Structural & Molecular Biology, 26(3)

### ISSN

1545-9993

### Authors

Nair, Sreejith J  
Yang, Lu  
Meluzzi, Dario  
[et al.](#)

### Publication Date

2019-03-01

### DOI

10.1038/s41594-019-0190-5

Peer reviewed



Published in final edited form as:

*Nat Struct Mol Biol.* 2019 March ; 26(3): 193–203. doi:10.1038/s41594-019-0190-5.

## Phase separation of ligand-activated enhancers licenses cooperative chromosomal enhancer assembly

Sreejith J. Nair<sup>1,\*</sup>, Lu Yang<sup>1,6</sup>, Dario Meluzzi<sup>1,6</sup>, Soohwan Oh<sup>1,2,6</sup>, Feng Yang<sup>1,6</sup>, Meyer J. Friedman<sup>1</sup>, Susan Wang<sup>1,3</sup>, Tom Suter<sup>1</sup>, Ibraheem Alshareedah<sup>4</sup>, Amir Gamliel<sup>1</sup>, Qi Ma<sup>1</sup>, Jie Zhang<sup>1</sup>, Yiren Hu<sup>1,2</sup>, Yuliang Tan<sup>1</sup>, Kenneth A. Ohgi<sup>1</sup>, Ranveer Singh Jayani<sup>1</sup>, Priya R. Banerjee<sup>4</sup>, Aneel K. Aggarwal<sup>5</sup>, Michael G. Rosenfeld<sup>1,\*</sup>

<sup>1</sup>Howard Hughes Medical Institute, Department and School of Medicine, University of California, San Diego, La Jolla, CA, USA.

<sup>2</sup>Biological Sciences Graduate Program, University of California, San Diego, La Jolla, CA, USA.

<sup>3</sup>Cellular and Molecular Medicine Graduate Program, University of California, San Diego, La Jolla, CA, USA.

<sup>4</sup>Department of Physics, University at Buffalo—SUNY, Buffalo, NY, USA.

<sup>5</sup>Department of Pharmacological Sciences, Icahn, School of Medicine at Mount Sinai, New York, NY, USA.

<sup>6</sup>These authors contributed equally: Lu Yang, Dario Meluzzi, Soohwan Oh, Feng Yang.

### Abstract

A crucial feature of differentiated cells is the rapid activation of enhancer-driven transcriptional programs in response to signals. The potential contributions of physicochemical properties of

---

\*Correspondence and requests for materials should be addressed to S.J.N. or M.G.R. sjnair@ucsd.edu; mrosenfeld@ucsd.edu. Author contributions

S.J.N., LY. and M.G.R. designed the experimental strategies. D.M. generated codes and carried out informatics analyses on FISH images. S.J.N. and J.Z. performed FISH experiments, vector design and cloning. F.Y. performed CHIP-seq analyses and GATA3 mutation studies with S.J.N. D.M., Y.T. and Q.M. performed the bioinformatics analyses. S.O. performed 4 C and GRO-seq assays. S.W. and T.S. performed live-cell imaging. A.G. performed the in situ Hi-C. S.J.N., F.Y. and Y.H. carried out the knockdown experiments. M.F. purified proteins for in vitro assays. P.R.B. and I.A. performed in vitro phaseseparation assays, FRAP and data analysis. R.S.J. performed ATAC-Seq. K.O. prepared samples for deep sequencing. S.J.N. carried out the b-isox precipitation assay, 1,6-HD experiments and optodroplet assays. S.J.N. and M.G.R. conceived and supervised the project. S.J.N. and M.G.R. wrote the manuscript with input from P.R.B., A.K.A., L.Y. and D.M.

#### Competing interests

The authors declare no competing interests.

**Supplementary information** is available for this paper at <https://doi.org/10.1038/s41594-019-0190-5>.

**Reprints and permissions information** is available at [www.nature.com/reprints](http://www.nature.com/reprints).

**Publisher's note:** Springer Nature remains neutral with regard to jurisdictional claims in published maps and institutional affiliations.

The authors declare no conflict of interests.

#### Data availability

Next-gen sequencing data sets generated from this study can be accessed at GEO using accession ID GSE99544. Distance measurements from microscopy experiments are included in this published article (and its supplementary information files). All data sets and code used in this study are available from the corresponding author upon reasonable request.

#### Online content

Any methods, additional references, Nature Research reporting summaries, source data, statements of data availability and associated accession codes are available at <https://doi.org/10.1038/s41594-019-0190-5>.

enhancer assembly in signaling events remain poorly understood. Here we report that in human breast cancer cells, the acute  $17\beta$ -estradiol-dependent activation of functional enhancers requires assembly of an enhancer RNA-dependent ribonucleoprotein (eRNP) complex exhibiting properties of phase-separated condensates. Unexpectedly, while acute ligand-dependent assembly of eRNPs resulted in enhancer activation sensitive to chemical disruption of phase separation, chronically activated enhancers proved resistant to such disruption, with progressive maturation of eRNPs to a more gel-like state. Acute, but not chronic, stimulation resulted in ligand-induced, condensin-dependent changes in spatial chromatin conformation based on homotypic enhancer association, resulting in cooperative enhancer-activation events. Thus, distinct physicochemical properties of eRNP condensates on enhancers serve as determinants of rapid ligand-dependent alterations in chromosomal architecture and cooperative enhancer activation.

## Reporting Summary.

Further information on research design is available in the Nature Research Reporting Summary linked to this article.

---

Enhancers serve as critical regulatory elements for transcriptional programs by directing development, homeostasis and disease states<sup>1,2</sup>. Clusters of enhancers located in a relatively small genomic region, known as super enhancers<sup>3,4</sup> or stretch enhancers<sup>5</sup>, exhibit more regulatory potential than individual enhancers by acting in a cooperative fashion<sup>6–8</sup>. The underlying mechanism for the enhancer function and cooperativity of super enhancers has been proposed to be the physical process of liquid-liquid phase separation (LLPS)<sup>9,10</sup>. LLPS is characterized by spontaneous demixing of a homogenous solution into two phases of high and low concentrations, and has been attributed to the assembly of several membrane-less organelles<sup>11–13</sup>. In support of this model, intrinsically disordered regions (IDRs) of transcriptional cofactors associated with clustered enhancers in embryonic stem cells are capable of liquid phase condensation at active super enhancers<sup>14,15</sup>. Key tissue-specific transcription factors also undergo phase separation in vitro and condensate formation in vivo on super enhancers<sup>16</sup>. Recent studies have also linked low complexity activation domains of transcription factors, cofactors and RNA polymerase II, with gene regulation<sup>17–21</sup>.

Other characteristics of enhancers that may be explained by LLPS model of enhancer assembly are the extent and rapidity of their response to specific signals. For example,  $17\beta$ -estradiol ( $E_2$ ) can coordinate genome-wide transcriptional programs through acute, signal-induced activation of enhancers that exhibit minimal basal activity<sup>22,23</sup>. In response to  $E_2$ , robust enhancers bound to estrogen receptor  $\alpha$  ( $ER\alpha$ ) transcribe high levels of enhancer RNAs (eRNAs)<sup>23–26</sup>, which are a class of long noncoding RNA transcribed from the core of functionally active enhancers<sup>27,28</sup>. A key feature of the most robust  $E_2$  responsive enhancers is the recruitment of an  $ER\alpha$ -dependent, megadalton-scale protein complex, referred to as the MegaTrans complex<sup>25</sup>. This complex is characterized by trans-recruitment of DNA-binding transcription factors such as GATA3,  $RAR\alpha/\gamma$ ,  $AP2\gamma$ , c-Jun, c-Fos, STAT1 and FOXA1, and enzymatic machinery including DNA-dependent protein kinase. Many components of this complex harbor IDRs, consistent with the overrepresentation of low complexity sequences in the activation domains of transcription factors<sup>29,30</sup>. The resulting high local concentration of eRNA together with a complex composed of several transcription

factors would appear to provide a conducive microenvironment for the assembly of eRNP condensates that effectively regulate signal-inducible transcription.

Assembly of transcription machinery as biomolecular condensates on most active enhancers raises several interesting questions. For example, is there a distinction in the biophysical properties of the transcription complex condensates assembled at enhancers with respect to the duration of ligand and/or signal activation? Do phase-separated condensates facilitate alterations of three-dimensional chromosomal architecture? What is the functional implication of this process in signal-induced transcriptional programs? Here, we report that the most robust E<sub>2</sub>-responsive enhancers recruit several proteins harboring IDRs that can undergo LLPS both in vitro and in vivo. Unexpectedly, the acutely activated enhancers, but not those exposed to chronic stimulation by ligand or constitutively activated enhancers, exhibit assembly of eRNP condensates with physicochemical properties of dynamic liquid droplets. The dynamic nature of eRNPs is linked to signal-induced proximity and cooperative activation of enhancers separated by vast genomic distances.

## Results

### MegaTrans enhancer proteins form phase-separated liquid droplets.

Estrogen signaling activates 7,000–8,000 enhancers genome-wide, out of which 1,248 are exceptionally active, on the basis of eRNA transcription and regulatory potential<sup>23,25,31</sup>. These exceptionally active enhancers are characterized by E<sub>2</sub>-dependent recruitment of high levels of ER $\alpha$ , RNA PolIII, MegaTrans components (for example, GATA3, FOXA1 and AP2 $\gamma$ )<sup>25,31,32</sup>, MED1 and P300 (schematics in Fig. 1a, Supplementary Fig. 1a and Supplementary Table 1) and by higher induced chromatin openness when compared to weak ER $\alpha$ -bound enhancers (Supplementary Fig. 1b). These robustly E<sub>2</sub>-activated enhancers are referred to here as MegaTrans enhancers. Sequence analysis of protein components of the complex bound to MegaTrans enhancers (termed the MegaTrans complex) revealed that several components (namely, GATA3, ER $\alpha$ , RARA, FOXA1, AP2 $\gamma$ , SMC4) contain stretches of amino acids predicted to form IDRs (Supplementary Fig. 2a). Consistently, these MegaTrans components were precipitated from nuclear lysates in the presence of biotinylated isoxazole (b-isox), a compound known to precipitate proteins containing low complexity domains or IDRs<sup>33</sup> (Fig. 1b). GATA3, a central component in the assembly of the MegaTrans complex<sup>25</sup>, harbors the highest percentage of disorder among the analyzed proteins (Supplementary Fig. 2a) and was consistently precipitated with the lowest concentration of b-isox (Fig. 1b).

The presence of IDRs in MegaTrans components suggests that they may form phase-separated condensates. To investigate this possibility using prototypic MegaTrans components, we purified ER $\alpha$  and GATA3 as holoproteins fused to MBP and mixed each protein with 5% polyethylene glycol (PEG), a crowding agent. Confocal microscopy imaging of these mixtures revealed the formation of micron-sized droplets (Supplementary Fig. 2b). In contrast, such droplets were not observed with MBP alone under identical experimental conditions. Both GATA3 and ER $\alpha$  condensates exhibited typical characteristics of phase-separated liquid droplets, such as spherical aspect ratio (Supplementary Fig. 2c) and propensity to coalesce (Supplementary Videos 1 and 2).

To further probe the fluid properties of the condensates, we employed fluorescence recovery after photobleaching (FRAP)<sup>34</sup> as a tool to study protein diffusion in droplets. For FRAP experiments, we used a total protein concentration of 7–10  $\mu\text{M}$ , ~1% of which was labeled with a fluorescent dye<sup>35</sup>. Both GATA3-MBP and ER $\alpha$ -MBP droplets showed almost full recovery (~90%) of bleached fluorescence within 100–400 s, suggesting that the condensed protein phases are viscous liquids<sup>36</sup> (Fig. 1c,d). The difference in recovery kinetics between GATA3-MBP and ER $\alpha$ -MBP droplets ( $t_{1/2}$  of  $100 \pm 6$  s versus  $24 \pm 2$ ) is probably due to the distinct nature and strength of weak multivalent interactions<sup>37</sup>, as the two proteins possess very different amino acid sequences and structures. Additionally, when GATA3-MBP and ER $\alpha$ -MBP were mixed together in vitro, two-color confocal microscopy analysis revealed that they are enriched and coexist in a single, phase-separated condensate, with the concentration of ER $\alpha$  considerably higher in the interior of the GATA3 droplet than at the dispersed phase (Supplementary Fig. 2d).

To examine the in vivo phase separation capability of the IDRs of GATA3 and ER $\alpha$ , we employed the optodroplet assay, a light activated system to study IDR mediated condensation in cells<sup>38</sup>. IDRs of both GATA3 and ER $\alpha$  fused to mCherry-Cry2 demonstrated efficient clustering and droplet formation on blue light stimulation and exhibited liquid droplet fusion behavior in HEK293 cells (Supplementary Fig. 2e–g and Supplementary Videos 3 and 4). Cry2-mCherry alone showed no clustering activity under the same exposure settings (Supplementary Fig. 2e and Supplementary Video 5). These results support the notion that the IDRs of GATA3 and ER $\alpha$  are capable of forming phase-separated droplets in vivo.

Because GATA3 and ER $\alpha$  are robustly recruited to MegaTrans enhancers on stimulation by  $E_2$ , we asked whether enhancer-bound MegaTrans holoproteins could also undergo clustering in vivo. To visualize such clusters, we fused ER $\alpha$  with monomeric-mCherry at the N terminus and expressed the fluorescently labeled protein in MCF7 cells. Live-cell imaging revealed acute assembly of nuclear ER $\alpha$  foci within 1 min after  $E_2$  treatment in ~80% of the cells (Fig. 1e and Supplementary Video 6), with an average of  $121 \pm 25$  distinct foci per nucleus, whereas no ER $\alpha$  foci were observed before  $E_2$  treatment. We obtained identical results using ER $\alpha$  labeled with mTurquoise, a different monomeric fluorophore (Supplementary Video 6). To examine the physical association of these  $E_2$ -dependent ER $\alpha$  condensates with MegaTrans enhancer targets, we carried out RNA fluorescence in situ hybridization (FISH) experiments on cells displaying ER $\alpha$ -mCherry foci. RNA FISH using probes targeting *TFF1* introns, which is ~9 kb from the corresponding MegaTrans enhancer, appeared in close proximity to ER $\alpha$  foci (Supplementary Fig. 3a,b). In contrast, the transcribing loci of *DYRK1A*, which does not depend on  $E_2$ , appeared at a much greater distance from ER $\alpha$  foci (Supplementary Fig. 3a,b). These data support the hypothesis that at least a subset of ER $\alpha$  foci develops in proximity to MegaTrans enhancers. We next examined the physical properties of ER $\alpha$  foci that formed after 1 h  $E_2$  treatment, with a median radius of ~0.96  $\mu\text{m}$ . FRAP experiments revealed fluorescence recovery with half-life of  $15.6 \pm 1.07$  s (Fig. 1f and Supplementary Fig. 3c) and apparent diffusion coefficient  $D_{\text{app}}$  of ~0.04  $\mu\text{m}^2$  s. The  $D_{\text{app}}$  value is an order of magnitude lower comparable to previously reported in vivo FRAP data on transcription related proteins that form biomolecular

condensates<sup>15,39</sup>, potentially reflecting the difference in the dynamics with which ER $\alpha$  binds directly to consensus motifs in chromatin.

We next explored the possible involvement of IDRs in the function of MegaTrans enhancers *in vivo*. To probe the role of the IDR in GATA3, we expressed either the wild type protein or a mutant form lacking the IDR (aa 2–250, a length characteristic of transcription-factor IDRs) in MCF7 cells where endogenous *GATA3* had been depleted by targeting its 3' UTR with shRNA (Supplementary Fig. 3d,e). The E<sub>2</sub>-dependent activation of MegaTrans enhancers was then observed by measuring the expression of their eRNAs by quantitative PCR with reverse transcription (qRT-PCR). We found that the loss of E<sub>2</sub>-mediated activation of MegaTrans enhancers and their target genes was effectively rescued by expression of wild type GATA3, but not by the mutant protein lacking the IDR (Fig. 1g and Supplementary Fig. 3f).

Together, our data demonstrate that GATA3 and ER $\alpha$ , two key components recruited to the MegaTrans enhancers, are capable of phase separating *in vitro* and *in vivo*, forming functional condensates with distinct fluid dynamics at MegaTrans enhancer loci.

### Phase separation underlies enhanceosome assembly at acutely induced enhancers.

The association of MegaTrans enhancers with functional phase-separated condensates led us to wonder whether such condensates play a role in enhanceosome assembly and thus enhancer activity.

To address this question, we first examined eRNA transcription in the presence of 1,6-hexanediol (1,6-HD), an aliphatic alcohol that disassembles phase-separated ribonucleoprotein (RNP) granules and membraneless structures by disrupting weak hydrophobic interactions<sup>40,41</sup>. qRT-PCR analysis revealed that 1,6-HD considerably reduced E<sub>2</sub>-induced eRNA expression from selected MegaTrans enhancers, while no effect was observed by the similar aliphatic alcohols 2,5-hexanediol (2,5-HD) or 1,4-butanediol (1,4-BD), which have minimal impact on the phase behavior of disordered proteins<sup>40,41</sup> (Supplementary Fig. 4a).

To gather genome-wide data, we carried out global run-on sequencing (GRO-seq) analysis on MCF7 cells that were treated first with 1,6-HD or 2,5-HD for 5 min and then with E<sub>2</sub> for 30 min. The inhibitory effect of 1,6-HD on eRNA transcription was almost exclusively limited to the MegaTrans enhancers, with no effects on transcription from weak ER $\alpha$  enhancers or non-ER $\alpha$ -bound enhancers (Fig. 2a), in agreement with MegaTrans enhancers ranking amongst the most active enhancers in E<sub>2</sub>-treated cells<sup>23,24</sup>. These results suggest that 1,6-HD inhibited the functional assembly of the MegaTrans complex. To examine whether 1,6-HD could also disrupt the function of preassembled MegaTrans complex, the cells were treated first with E<sub>2</sub> for 1 h, thus ensuring MegaTrans assembly<sup>25</sup>, and then with 1,6-HD for 5 min. This experimental design also resulted in specific suppression of MegaTrans-bound enhancer transcription (Supplementary Fig. 4b), suggesting that 1,6-HD may disrupt the function of fully assembled MegaTrans complex. Suppression of E<sub>2</sub>-activated transcription was also evident at target coding genes of MegaTrans enhancers (Supplementary Fig. 4c).

To examine the impact of 1,6-HD on assembly of MegaTrans on chromatin, we carried out ChIP-seq experiments. While ER $\alpha$  was still effectively recruited to MegaTrans enhancers following 1,6-HD treatment (Fig. 2b), other MegaTrans component assembly was substantially disrupted, as evidenced by impairment of GATA3 and AP2 $\gamma$  recruitment to the complex (Fig. 2c,d). Therefore, 1,6-HD specifically disrupted the assembly of the trans-recruited complex. Similar results were also observed for RAR $\alpha$  on two examined MegaTrans enhancers (Supplementary Fig. 4d). Western blot analysis on control and 1,6-HD-treated samples, both stimulated with E<sub>2</sub>, revealed no impact of these treatments on cellular levels of ER $\alpha$ , GATA3 or AP2 $\gamma$  (Supplementary Fig. 4e). Exposure to 1,6-HD for 5 min also resulted in dramatic reduction in the number and signal intensity of induced ER $\alpha$ -mTurquoise foci (Fig. 2e), suggesting that these assemblies are also disrupted in parallel with transcriptional impact. These results indicate that phase separation dependent on hydrophobic interactions plays a role in the assembly of the MegaTrans complex and in acute activation of E<sub>2</sub>-stimulated enhancers.

The inferred involvement of phase separation with MegaTrans enhancers suggests the possibility that 1,6-HD sensitivity and LLPS are general properties of rapidly induced, signal-dependent enhancers. To test this hypothesis, we examined two other signaling programs that induce rapid activation of enhancers on stimulation: TNF $\alpha$ -mediated activation of NF- $\kappa$ B-bound enhancers in MCF7 cells<sup>42</sup> and Kdo2-lipid A (KLA)-stimulated Tlr-4 enhancers in mouse macrophage RAW264.7 cells<sup>43</sup>. TNF $\alpha$ -induced activation of NF- $\kappa$ B-dependent enhancers in MCF7 cells was sensitive to 1,6-HD, which affected only the most active NF- $\kappa$ B-dependent enhancers, with no effects on other enhancers, including those regulated by E<sub>2</sub>-stimulation (Fig. 2f). Similarly, the rapid, KLA-mediated activation of potent enhancers in mouse macrophage RAW264.7 cells was abrogated by treatment with 1,6-HD (Fig. 2g). eRNA transcription from other robust enhancers that are basally active was actually elevated in response to 1,6-HD (Fig. 2a,f,g and Supplementary Fig. 4b, third group in each panel). Together, these data reveal that the initial, signal-dependent nucleation of enhanceosome complexes on potent, acutely activated enhancers, but not on basally active enhancers, represents an assembly process that is sensitive to 1,6-HD and is thus probably driven by phase separation.

### **Phase separation underlies long-distance interactions and cooperative activation of acutely induced enhancers.**

Since phase-separated condensates are prone to interacting through coalescence<sup>44,45</sup>, we asked whether the putative phase-separation events affecting MegaTrans enhancers might promote spatial interactions between those enhancers. We investigated E<sub>2</sub>-induced changes in chromosomal architecture by examining potential long-range intra-chromosomal interactions of enhancers located on human chromosome 21, which harbors multiple MegaTrans enhancers (Fig. 3a). We first performed Hi-C on ER $\alpha$ -positive MCF7 cells. Contact maps at 1 Mb resolution with ~500 M assignable sequence reads revealed no effect of E<sub>2</sub> on A/B compartments or boundaries of topologically associated domains (TADs) (Supplementary Fig. 5a), but suggested an enrichment of interactions between broad and genomically distant regions on chromosome 21 (Supplementary Fig. 5b). To study enhancer interactions with greater precision, we carried out 4C-seq experiments using a viewpoint on



*TFF1e*. These experiments revealed E<sub>2</sub>-induced interaction between the *TFF1* and the *DSCAM-AS* enhancer regions, which are separated by 1.9 Mb and located in two different TADs (Supplementary Fig. 5c), suggesting that homotypic long-distance interactions may be a feature of MegaTrans enhancers.

We systematically examined other E<sub>2</sub>-induced changes in chromosome conformation along chromosome 21 using DNA FISH to quantitate pairwise distances between multiple enhancer regions. E<sub>2</sub> treatment for 50 min resulted in a subtle (5–17%) but consistent decrease in median spatial distances between several MegaTrans enhancer loci on chromosome 21, separated by 1.9–27 Mb, as evidenced by comparing cumulative distance distributions and median spatial distances (Fig. 3b,c, Supplementary Fig. 6a,b,c and Supplementary Table 2). In contrast, no E<sub>2</sub>-induced proximity was observed between MegaTrans enhancers and genomic regions devoid of ER $\alpha$  binding (*CP26* and *TFF1*, *CP26* and *NRIP1*, in Supplementary Fig. 6c), suggesting that E<sub>2</sub> specifically affects the spatial proximity of MegaTrans enhancers.

To examine the kinetics of such changes, we assessed the proximity of two regions by comparing their spatial distance to a cutoff value that depends on the genomic separation of those regions (Supplementary Fig. 6d and Supplementary Note). There was a roughly three-fold increase in the fraction of *TFF1* and *NRIP1* enhancer regions, separated by a genomic distance of 27 Mb, reaching spatial proximity (<600 nm) within 5 min of E<sub>2</sub> stimulation (Fig. 3d). The rapid kinetics observed for E<sub>2</sub>-induced proximity of specific ER $\alpha$  enhancers separated by vast genomic distances suggests a model of homotypic enhancer association driven by coalescence of ligand-induced enhancer condensates. Our experiments also revealed an asynchrony of transcriptional responses within 15 min of E<sub>2</sub> treatment, as RNA FISH data using intronic and exonic probes of *TFF1* and *NRIP1* demonstrated that only 20–30% of cells have active transcription (intronic probe) of these genes at a given time point, but roughly 55–75% of cells showed mature transcript (exonic probe) over the 15-min period of stimulation (Supplementary Fig. 7a–c). This supports the notion that the small changes in spatial proximity could be functionally relevant and is consistent with the relatively lower frequency of active transcriptional events observed.

### Functional consequences of E<sub>2</sub>-induced proximity of MegaTrans enhancers.

To assess the functional consequences of the E<sub>2</sub>-induced proximity between MegaTrans enhancers, we investigated the relationship between spatial proximity and transcriptional activity of their targets. The transcriptional activation of *NRIP1*, as quantified by measuring the fluorescence signal intensity of intronic RNA FISH probes, was inversely related to its spatial distance from *TFF1* (Fig. 3e,f). A similar relationship was observed for other ER $\alpha$  target pairs, such as *NRIP1-DSCAM-AS1* and *DOPEY2-TFF1* (Fig. 3f, Supplementary Fig. 7d,e and Supplementary Table 3), suggesting that E<sub>2</sub>-induced proximity of MegaTrans enhancers is correlated with cooperative activation of coding targets. To explore whether this induced proximity might require LLPS at the enhancers, we tested the impact of 1,6-HD on their spatial proximity. Indeed, 1,6-HD effectively attenuated the E<sub>2</sub>-induced proximity of *NRIP1* and *TFF1* enhancer regions (Fig. 3g), suggesting that the spatial proximity between



MegaTrans enhancers depends on cooperative homotypic interactions requiring eRNP complexes with the properties of phase-separated condensates.

Previous observations have suggested that such functionally important interactions between loci might involve their colocalization in subnuclear structures<sup>46,47</sup>. For example, enhancer and gene activation in cell lineage determination require interaction of a POU domain lineage-determining factor with the Matrin3 network<sup>48</sup> and possibly with the interchromatin granule (ICG)<sup>46,47,49</sup>, which is also a phase-separated RNP condensate<sup>50,51</sup>. Accordingly, we investigated the relation between ICGs and MegaTrans enhancers. RNA FISH using intronic probes revealed that the actively transcribed *NRIP1* and *TFF1* alleles associated with ICGs were roughly three times more active than the alleles not associated with ICGs (Supplementary Fig. 8a,b). Moreover, the transcriptional robustness of *NRIP1* was significantly higher when both *NRIP1* and *TFF1* were associated with the same ICG (Supplementary Fig. 8c,d), suggesting that association through ICGs may facilitate the cooperative activation of MegaTrans enhancers. Knockdown of *SRSF1* or *U2AF1* (Supplementary Fig. 8e), two ICG-associated splicing proteins<sup>52,53</sup>, resulted in attenuated transcription of eRNAs from MegaTrans enhancers (Supplementary Fig. 8f,g). Next, we evaluated the association of E<sub>2</sub>-induced ER $\alpha$  foci with ICGs by co-expressing SC35 (SRSF2)-RFP and ER $\alpha$ -mTurquoise in MCF7 cells and inducing the formation of ER $\alpha$  foci by E<sub>2</sub> stimulation. Microscopic analysis revealed that, among the observed ER $\alpha$  condensates, roughly 80% were located within 400 nm of an ICG (Fig. 3h and Supplementary Fig. 8h), providing evidence for the spatial proximity of E<sub>2</sub> induced ER $\alpha$  foci and MegaTrans enhancers with ICGs.

These results indicate that phase-separation events at enhancers, coupled with proximity to ICG condensates, underlie E<sub>2</sub>-induced alterations to chromosomal architecture and cooperative activation of distant MegaTrans enhancer loci.

### **eRNA and condensin recruitment are required for E<sub>2</sub>-induced MegaTrans enhancer proximity.**

A key feature of active regulatory enhancers, as exemplified by E<sub>2</sub>-stimulated enhancers, is production of eRNAs that are functionally important for target gene regulation<sup>23,28,54,55</sup>. Because a large proportion of phase-separated biomolecular condensates are assembled as RNP complexes<sup>13,51,56</sup>, we asked whether the observed phase-separation events at MegaTrans enhancers involve the formation of eRNA-containing RNPs. To test whether MegaTrans eRNAs affect the assembly of MegaTrans components, we carried out ChIP experiments in E<sub>2</sub>-treated cells after knocking down *TFF1*e eRNA with an antisense oligonucleotide (ASO) (Supplementary Fig. 9a). Depletion of *TFF1*e eRNA abolished recruitment of MegaTrans components GATA3, RAR $\alpha$  and AP2 $\gamma$  to *TFF1* enhancer region in response to E<sub>2</sub>, with no impact on the primary transcription factor, ER $\alpha$  (Fig. 4a). This result is reminiscent of the disruption of the assembly of trans-recruited MegaTrans components, but not direct DNA binding of ER $\alpha$ , by 1,6-HD (Fig. 2b–d) and supports a role for eRNAs in recruiting MegaTrans components. Moreover, E<sub>2</sub> stimulation of the eRNA-depleted cells failed to induce proximity between the *NRIP1* and *TFF1* regulatory regions

(Fig. 4b and Supplementary Fig. 9b), suggesting that MegaTrans eRNAs are also required for E<sub>2</sub>-induced proximity of MegaTrans enhancers.

To test whether eRNAs affect MegaTrans enhancers by altering the properties of phase-separated protein droplets, we mixed in vitro transcribed, fluorescently labeled *TFF1e* eRNA with purified ER $\alpha$ -MBP or GATA3-MBP fusion proteins, in the presence of 5% PEG and 200 mM NaCl. FRAP experiments revealed that *TFF1e* eRNA, but not control RNA, shortened the recovery time ( $t_{1/2}$ ) of GATA3-MBP fusion protein droplets by roughly 50% ( $100 \pm 6$  s to  $52 \pm 6$  s, comparable bleaching regions of interrogation, ROI) (Fig. 4c and Supplementary Fig. 9c,d). FRAP kinetics for ER $\alpha$ -MBP droplets also was reduced in the similar conditions (Fig. 4d and Supplementary Fig. 9e). These results suggest that the diffusion properties of phase-separated MegaTrans components are specifically affected by eRNAs transcribed from MegaTrans enhancers.

To further elucidate the interplay between eRNAs and MegaTrans enhancers, we directed our attention to condensins. This choice was motivated by previous reports that both condensin I and II complexes, but not cohesin, are robustly recruited to ER $\alpha$  enhancers in an E<sub>2</sub>-dependent manner in interphase MCF7 cells<sup>31</sup>. Here, analysis of ChIP-Seq data revealed a strong E<sub>2</sub>-dependent recruitment of both NCAPG (a condensin I subunit) and NCAPH2 (a condensin II subunit) to MegaTrans enhancers, but only minimal recruitment to weak ER $\alpha$ -bound enhancers and non-ER $\alpha$ -bound enhancers (Supplementary Fig. 9f). Moreover, ChIP of condensin components following depletion of eRNAs from *TFF1* and *NRIP1* enhancers (Supplementary Fig. 9g) significantly reduced the recruitment of NCAPG and NCAPH2 to those enhancers (Fig. 4e), indicating that their recruitment to the MegaTrans enhancers is eRNA-dependent. Thus, we asked whether condensins might serve as components of a phase-separated eRNP complex that induces proximity of MegaTrans enhancers on E<sub>2</sub> stimulation. SMC4, a component of the condensin complex, harbors an evolutionarily conserved IDR at its N terminus (Supplementary Fig. 2a) and was precipitated by biotinylated isoxazole (Fig. 1b), supporting the potential participation of the condensin complex in phase-separation events at MegaTrans enhancers. Moreover, following depletion of NCAPG or NCAPH2 (Supplementary Fig. 9h), FISH analysis revealed a significant reduction in E<sub>2</sub>-induced proximity between *NRIP1e* and *TFF1e* (Fig. 4f and Supplementary Fig. 9i). In contrast, depletion of cohesin subunit RAD21 produced only minimal effects (Fig. 4f and Supplementary Fig. 9i), suggesting that selective condensin recruitment to MegaTrans enhancers may be required for long-distance homotypic association. These results are consistent with the recently established ability of condensin to multimerize<sup>57</sup>. Furthermore, analysis of previously reported GRO-seq data after depletion of either NCAPG or NCAPD3<sup>31</sup> revealed that eRNA synthesis was specifically reduced at MegaTrans enhancers (Fig. 4g), suggesting a feed-forward effect of condensins on eRNA expression. Thus, in addition to their known roles in mitosis and meiosis<sup>58</sup>, gene regulation<sup>59–61</sup> and chromatin architecture<sup>61,62</sup>, condensins also appear to facilitate long-distance homotypic enhancer association and cooperative activation of eRNP complexes at robust E<sub>2</sub>-regulated enhancers.

### Chronic stimulation by E<sub>2</sub> alters visco-elastic properties of MegaTrans enhancers and their effects on chromosomal architecture.

The observation that disruption of transcription by 1,6-HD was restricted to signal-induced enhancers and did not affect constitutively active enhancers (Fig. 2a,f,g and Supplementary Fig. 4b, third group in each panel) suggested a possible distinction in physicochemical properties between acutely and chronically activated enhancers. To investigate this possibility, we reasoned that continuous stimulation of MegaTrans enhancers by E<sub>2</sub> for a prolonged period of time might impart those enhancers with biophysical properties resembling those of RNP complexes at constitutively active enhancers. We thus chronically activated MCF7 cells by culturing them in E<sub>2</sub>-containing medium for 14–16 h. GRO-seq meta-analysis of cells treated with 2,5-HD or 1,6-HD after prolonged treatment with E<sub>2</sub> indicated that the active MegaTrans enhancers were no longer sensitive to 1,6-HD (Fig. 5a). Thus, chronic enhancer activation would appear to alter the biophysical properties of eRNPs at MegaTrans enhancers, compared to acute activation. These data, along with the lack of impact of 1,6-HD on constitutively active enhancers, also argue against an indiscriminate inhibition of transcription by 1,6-HD.

ChIP assays revealed a comparable level of recruitment of MegaTrans component RAR $\alpha$  at *TFF1e* and *NR1P1e* enhancers after short-term (30 min) and long-term (14 h) E<sub>2</sub> treatment (Supplementary Fig. 10a). In contrast, GRO-seq data revealed that the level of induction of E<sub>2</sub> target genes by chronic E<sub>2</sub> treatment, although significantly higher than basal level, was lower than the induction by acute treatment of the ligand (Supplementary Fig. 10b). This suggests that 1,6-HD-insensitive MegaTrans assembly was not as transcriptionally competent as the complex assembled on acute stimulation. To test the ligand responsiveness of complexes after long-term treatment, we treated the 14 h E<sub>2</sub>-stimulated cells with one more dose of E<sub>2</sub> for 1 h. GRO-seq analysis between these two conditions revealed only minor differences in the transcription level (Supplementary Fig. 10c). These data further support the idea that MegaTrans enhancers after long-term activation are not as transcriptionally competent as short-term activated enhancers.

This finding motivated us to explore the effects of prolonged E<sub>2</sub> stimulation on the biophysical properties of eRNP assembly. We induced ER $\alpha$ -Turquoise foci in MCF7 cells by short-term (30 min) and long-term (16 h) treatment with E<sub>2</sub>. FRAP analysis revealed a significantly slower recovery of photobleached foci after long-term treatment in comparison to short-term treatment with E<sub>2</sub> (Fig. 5b and Supplementary Fig. 10d). The time constants derived from these two conditions were also significantly different (Fig. 5c), suggesting distinct physicochemical properties imparted by different activation regimen. We further examined the distinction between acute and chronic phase-separation events in vitro by mixing GATA3, ER $\alpha$  and in vitro transcribed *TFF1e* eRNA. The FRAP kinetics of the resulting droplets were then measured at 5, 90 and 180 min after the assembly. Consistent with the in vivo observations, the rapid FRAP kinetics observed on immediate droplet formation of this ternary mixture in vitro was diminished at 90 min and dramatically slowed at 180 min (Fig. 5d). In addition, immediately assembled droplets were more sensitive to 1,6-HD when compared to the mature droplets (Supplementary Fig. 10e). These data are consistent with an alteration in the visco-elastic properties of eRNP condensates at

MegaTrans enhancers after long-term E<sub>2</sub> treatment and support a model in which the eRNP complex progressively transitions from a fluid to a more viscous gel-like or solid state.

We asked whether chronic E<sub>2</sub> stimulation might also affect induced enhancer proximity observed after acute stimulation. We determined the spatial proximity of MegaTrans enhancer loci using DNA FISH probes targeting two different enhancer pairs, *TFF1e/NR1P1e* and *TIAM1e/DSCR3e*. We found that the spatial proximity observed after 50 min of E<sub>2</sub> treatment was no longer observed after 16 h treatment (Fig. 5e), indicating that chronic activation abolishes E<sub>2</sub>-induced proximity of MegaTrans enhancers. This is consistent with the GRO-seq data indicating the attenuated transcriptional response after long-term E<sub>2</sub> stimulation (Supplementary Fig. 10c).

These data indicate the importance of the physicochemical properties of MegaTrans condensates in the functional behavior of ER $\alpha$  enhancers, highlighting the distinction between acute and chronic E<sub>2</sub> stimulation with respect to transcriptional activation and chromosomal architecture.

## Discussion

Here, we provide evidence that acute enhancer activation by E<sub>2</sub> ligand and other signaling pathways results in eRNA-mediated RNP assembly displaying properties of phase-separated condensates at the most robust ER $\alpha$  enhancers. This assembly is apparently required for cooperative activation of these enhancers on the basis of homotypic enhancer interactions spanning multiple TADs, altering chromosomal architecture. It has recently been discovered that phase-separated condensates can exert forces on their associated chromatin, causing two distal telomere loci to be brought into close proximity<sup>45</sup>. We propose that the strongest MegaTrans enhancers such as *NR1P1e* and *TFF1e* can bring their genomic loci into proximity with other MegaTrans enhancers using a similar mechanism. Optimal cooperative activation of these enhancers is further augmented by the ability of the enhancer loci to interact with ICGs, which are also membraneless RNP condensates<sup>50,51</sup> (Supplementary Fig. 8a,b), thereby potentially increasing local cofactor concentration and retention time. The observed effect of 1,6-HD on disruption of ligand-induced MegaTrans enhancer proximity and activation strongly suggests that the MegaTrans eRNP complex is also a condensate organized by hydrophobic interactions.

A striking observation in this context is that constitutively active enhancers or MegaTrans enhancers chronically stimulated by E<sub>2</sub> did not show comparable sensitivity to inhibition by 1,6-HD. This reduced sensitivity is consistent with less dynamic ER $\alpha$  foci in vivo and eRNP condensates in vitro after prolonged stimulation, suggesting an ‘aging’ mechanism that is reminiscent of the time- and concentration-dependent physicochemical transition observed with RNA-binding proteins<sup>63,64</sup>. The consequence of such an altered state is that chronically stimulated enhancers no longer exhibit ligand-induced spatial proximity and cooperativity across the chromosome. At a functional level, these enhancers are transcriptionally less active compared to the acutely activated state, and are not responsive to further stimulation.

Drawing a parallel from recent findings on the surface tension driven coalescence of genomic loci<sup>45</sup>, we speculate that the physical force driving the long-distance signal-induced enhancer proximity is the liquid surface tension of the MegaTrans condensates, a property that might be lost as condensates undergo transition to a more solid and less dynamic state over time. The liquid-to-solid transition of the RNA-binding protein FUS has been compared to the process of protein crystallization, whereby the metastable liquid phase triggers nucleation of a higher order assembly<sup>64</sup>. We also consider the possibility of a conformational transition or the sampling of different conformations and interactions of the protein and RNA components over time. We therefore propose that ligand-activated, newly formed eRNP structures behave as metastable liquid droplets, governed by weak protein-protein, RNA-RNA and protein-RNA interactions, which, on prolonged activation, may mature to a thermodynamically favorable, less fluid, 'hydrogel-like' state<sup>33,63-65</sup> (Fig. 6).

An issue that has remained unresolved is how eRNAs might alter the physical properties of condensates assembled on enhancers. In addition to its requirement for full assembly of MegaTrans enhancers, we have found that eRNA promotes a more dynamic liquid-like state in GATA3 condensates in vitro (Fig. 4c). We propose that this eRNA-dependent increase in fluidity may assist in the coalescence of phase-separated enhancer condensates, not only across multiple TADs, but also with subnuclear structures such as ICGs. In summary, our model (Fig. 6) features temporal changes for the physicochemical properties of ligand-dependent MegaTrans eRNP condensates: at first, these condensates exhibit dynamic cooperative spatial association, capable of altering chromosomal architecture at a global level, but they eventually solidify into independent, autoregulatory transcriptional crucibles that have lost their homotypic interaction properties.

## Methods

### **Antibodies, cell culture, molecular biology procedures, sequencing-based assays.**

Antibodies, cell culture, molecular biology procedures (qRT-PCR, ChIP-seq and analyses; in vitro transcription; run-on sequencing; vector constructs), bioinformatics of enhancer characterization, generation of cell lines, protein purification, proximity calculation using microscopy data, In situ Hi-C, Hi-C data analysis, 4C-seq and ATAC-seq are described in detail in the Supplementary Note. Oligos, BAC and Fosmid clones are listed in Supplementary Tables 4 and 5.

### **Treatment of cultured cells.**

Cells were cultured as described in the Supplementary Note. For hexanediol treatment, cells were treated with 7.5–8.5% 1,6-Hexanediol (1,6-HD) (Sigma, catalog no. 240117), 2,5-hexanediol (2,5-HD) (Sigma, catalog no. H11904) or 1,4-butanediol (1,4-HD) (Sigma, catalog no. 493732) in phenol-red free DMEM with 5% charcoal stripped fetal bovine serum (FBS) (White medium) for 5 min. The chemical was washed away with white medium and was incubated with estrogen (100 nM) or vehicle for another 30 min at 37 °C before fixing with formaldehyde (for FISH), collecting RNA or nucleus for GRO-seq. In E2 pretreatment experiments, MCF7 cells were stimulated with E2 for indicated time periods followed by treatment with 2,5-HD or 1,6-HD for 5 min before the collecting nucleus for GRO-seq. For TNF $\alpha$  stimulation, MCF7 cells were grown as described for E2 stimulation and were treated

with 8% 1,6-HD or 2,5-hexanediol for 5 min followed by stimulation by 100 nM TNF $\alpha$  for 30 min before collecting the nucleus for GRO-seq. For KLA treatment, RAW264.7 cells were grown in DMEM media with 10% FBS. Cells were grown in medium with 0.5% serum overnight before KLA stimulation. Cells were treated with 8.5% 1,6-HD for 5 min before stimulation with 100 nM KLA for 30 min.

### **Biotinylated isoxazole-mediated precipitation.**

This assay was carried out as described previously<sup>33</sup> with following modifications. MCF7 cells cultured in phenol-red free media with charcoal stripped serum were stimulated with E<sub>2</sub> (100 nM) for 50 min. Roughly 15 million cells were scraped off with cell lifter and washed with ice cold PBS. Cell pellets were resuspended in 1 ml lysis buffer (20 mM Tris-HCl (pH 7.4), 300 mM NaCl, 5 mM MgCl<sub>2</sub>, 1% NP40, 10% glycerol, 20 mM P-mercaptoethanol, 1 $\times$  Halt protease/phosphatase inhibitor cocktail (Thermo Fisher, catalog no. 78440), 2 mM ribonucleoside vanadyl complexes (Sigma, catalog no. R3380), 0.1 mM phenylmethylsulfonyl fluoride (PMSF), 1:20 SuperaseIn (Thermo Fisher, catalog no. AM2696). Sonicated briefly on Bioruptor Pico (30 s on, 30 s off, five cycles) and incubated with rotation at 4 °C for 30 min. Protein supernatant was collected by centrifugation at 4 °C, 16,500g for 15 min. Then, 5% lysates were saved for whole cell extract control and remaining were aliquoted equally and incubated with various concentrations (10, 30 and 100  $\mu$ M) biotinylated isoxazole (Sigma, catalog no. 900572) at 4 °C for 1 h with rotation. Precipitates were isolated by centrifugation at 16,500g for 15 min at 4 °C. Supernatant was saved and pellets were washed with lysis buffer with protease and RNase inhibitor. Protein was denatured by heating at 98 °C for 5 min with Laemmli buffer with 0.1 M dithiothreitol. Western blotting was carried out by standard protocol.

### **Protein sequence analysis.**

The protein sequence from the Uniprot database was analyzed using Predictor of Natural Disordered Region (PONDR), online analysis software (v.VL3).

### **In vitro fluorescence labeling of proteins.**

The ER $\alpha$ -MBP and GATA3-MBP were fluorescently labeled with either Alexa488 or Alexa594 dyes (C5-maleimide derivative, Molecular Probes) using Cys-maleimide chemistry as described previously<sup>35</sup>. Both ER $\alpha$  (C381, C417, C447, C530) and GATA3 (C85, C183, C249, C375) contain four free cysteines, respectively, that were targeted for fluorescence labeling. The proteins containing the MBP fusion tag, which lacks cysteine, and the dye mixtures (1:4) were incubated in 25 mM Tris buffer, 50 mM NaCl, pH 7.5 at 4 °C for ~12 h. The unreacted dye was removed using a 30 kDa molecular weight cut-off (MWCO) spin filter. The labeling efficiency for all samples were observed to be 50% (ultraviolet-visible absorption measurements) and no additional attempt was made to purify them further, given that only labeled protein is observed in the fluorescence microscopy experiments. For control experiments with MBP-alone sample, we used the same fluorescently tagged proteins for fluorescence microscopy experiments. Simultaneously, we used bright-field microscopy to check droplet formation. Our results revealed that the MBP-alone sample did not become phase-separated under similar experimental conditions, which is consistent with a recent report<sup>17</sup>.



### Sample preparation for phase-separation measurements.

All of the protein samples were buffer exchanged in phase-separation buffer (25 mM Tris HCl, pH 7.5 containing 200 mM NaCl) unless otherwise noted. Concentration measurements were made using a NanoDrop oneC ultraviolet-visible spectrophotometer at room temperature. Variable amount of salt (NaCl) and PEG 8000 were added from concentrated stocks as indicated. For microscopy experiments using the MBP fusion proteins, buffer containing either 5 or 8.75% PEG was used.

### Confocal fluorescence microscopy.

Fluorescence and DIC imaging were performed using a Zeiss LSM 710 laser scanning confocal microscope, equipped with a  $\times 63$  oil immersion objective (Plan-Apochromat  $\times 63/1.4$  oil DIC M27) and a Zeiss Primovert inverted microscope. Samples were prepared and imaged using tween-coated (20% v/v) Nunc Lab-Tek Chambered Coverglass (Thermo Fisher Scientific Inc.) at room temperature ( $22 \pm 1$  °C) unless otherwise noted, with  $\sim 1\%$  labeled protein samples within the mixture of unlabeled materials. All the samples were allowed to equilibrate in the chambered coverglass for 15–30 min before imaging. For Alexa488-labeled samples the excitation and emission wavelengths were 488 nm or 503–549 nm, and for Alexa594-labeled samples the excitation and emission wavelengths were 595 nm or 602–632 nm. FRAP experiments were carried out using the same confocal set up. The bleaching ROI was  $\sim 1.0 \mu\text{m}^2$  unless otherwise noted. The samples were bleached using either five or ten iterative pulses of a total time  $\sim 3.0$ – $6.5$  s using 100% laser power. Analyses were carried out using average fluorescence intensities from three ROI corresponding to photobleaching, reference and background. The fluorescence signal of the protein droplet undergoing active photobleaching was corrected using the reference droplet signal to account for passive photobleaching during imaging. The fluorescence data were normalized and fitted with a two-exponential model<sup>66</sup>. Half-time of recovery was then obtained graphically. The images and data were analyzed using Fiji software<sup>67</sup> and the FRAP curves were plotted and analyzed using origin software (OriginPro 2016).

### ER $\alpha$ foci formation assay.

MCF7 cells were plated at 75% confluency 1 day before transfection. Then, 0.75  $\mu\text{g}$  of pmCherry-ESR1 (ER $\alpha$ ) plasmid was transfected using Lipofectamine 2000 (Thermo Fisher) per 24 wells, and the cells were incubated in the transfection mixture for 6 h. The cells were then washed and cultured in phenol-red free DMEM white medium (Life Technologies) supplemented with 5% charcoal stripped FBS. Transfected cells were re-plated into glass-bottom 96-wells (MatTek) the following day and cultured in DMEM white medium with 5% charcoal stripped FBS for another 24 h before imaging. Zeiss LSM 880 Airyscan was equipped with a CO<sub>2</sub> regulated incubation chamber (Incubator XL S1) where the ambient temperature was held at 37 °C. mCherry was excited using a diode-pumped solid state laser (Laser Line) at 561 nm and images were acquired in FAST Airyscan mode. A Z-stack of fluorescent MCF7 cells transfected with pmCherry-ESR1 were first imaged for 15 min at 5-min intervals to acquire a baseline readout of ER $\alpha$  expression. The cells were then immediately treated with 100 nM 17 $\beta$ -estradiol (E<sub>2</sub>) for estrogen stimulation and imaged consecutively for 1 h at 5-min intervals. Images acquired were compiled, processed and



edited with ZEN software (Zeiss). Intensity thresholds were set manually and uniformly to display nuclear signal and minimize background noise.

### FRAP assay and analysis in live cells.

MCF7 were transfected with pmTurquoise2-ESR1 and prepared for microscopy in identical conditions to those of the ER $\alpha$  Foci Formation Assay, with pmTurquoise2-ESR1 being used in place of pmCherry-ESR1. Before performing FRAP, cells were either untreated, pretreated with 16 h of 100 nM E<sub>2</sub>, or were treated with 100 nM E<sub>2</sub> immediately before FRAP. FRAP data for each condition was acquired over the course of approximately 1 h, with the results being combined for each condition as no trend was observed between FRAP data acquired at the beginning versus the end of the hour. FRAP was performed on the Zeiss LSM 880 Airyscan, under the same incubation conditions as before. Bleaching of the pmTurquoise2-ESR1 signal was carried out using the 405 nm laser at maximum strength, with two identical size regions selected for bleaching per cell. Fluorescence signal was acquired through excitation using laser line Argon at 458 nm, and mTurquoise2-ESR1 intensity was acquired in ZEN Black at the bleached regions, a control non-bleached region of the nucleus, a control region outside of the cells and over the entirety of each cell. Two baseline images were taken 3 s apart, which was followed by approximately 0.4 s of bleaching. Afterward, an image was taken immediately and then every 3 s until either a total of 60 images were acquired or the cell shifted planes dramatically.

### Analysis of in vivo FRAP data.

Analysis was carried out by first normalizing the intensity of each bleached spot's average intensity at each time point to the maximum intensity of that spot at any point in the time series. This point of maximum intensity was one of the baseline points, and each time point was converted to a proportion of the original intensity. The total intensity of each cell at each time point was normalized as a proportion of the maximum intensity of the total cell at any time point, thereby providing a value for the proportion of photobleaching of the total cell at each time point. The maximum-intensity normalized value of each bleached region at each time point was then divided by the total cell photobleaching proportion at its respective cell and time point. These maximum-intensity and photobleaching normalized values were then either plotted or used to generate time constants. Mean graphs with error bars for these normalized values were generated by calculating mean and standard error over all overlapping time points for all traces for each condition. Exponential rise curve plots contain each time point from all traces combined for each condition, time 0 was set as the time point acquired immediately after photobleaching and the average intensity value of this new time point 0 was subtracted from all intensity values for this condition to set the intensity offset to zero. These pooled points were fitted to an exponential rise curve with the formula  $FRAP(t) = A(1 - e^{-t/\tau})$ , where  $FRAP(t)$  is the fluorescent intensity at time  $t$  after photobleaching,  $A$  is the amplitude,  $\tau$  is the time constant and  $t$  is the time after photobleaching. The time constant and amplitude were optimized to fit the curve by subtracting the formula values from the actual values of each point, squaring this error value, summing the error of all the points for each condition and optimizing for amplitude and the time constant using the Solver add-in in Microsoft Excel. Box plots comparing between FRAP time constants of short versus long-term 100 nM E<sub>2</sub> treatment of ER-mTurquoise2 MCF7 cells were generated

by calculating time constants for each individual trace. These calculations were performed as in the above plot, except traces were not pooled for each condition and the intensity offset value subtracted from each intensity value for each trace was the intensity value of each trace immediately after photobleaching. A *P* value comparing between the short and long-term FRAP constants was generated by performing a two-tailed *z*-test between the two samples for means. The apparent diffusion coefficient was calculated by the formula  $D_{app} = r_{bleach}^2 / \tau$ , where  $D_{app}$  is the apparent diffusion coefficient,  $r_{bleach}^2$  is the radius of the bleached region in each FRAP experiment and  $\tau$  is the time constant calculated in the previous experiment. The radius of each bleached region for every FRAP experiment was set uniformly to 0.964  $\mu\text{m}$ .

### SC35 colocalization calculation.

MCF7 were co-transfected as before in the ER $\alpha$  foci formation assay, except 0.375  $\mu\text{g}$  pDsRed2-SC35 and 0.375  $\mu\text{g}$  pmTurquoise2-ESR1 were used in place of 0.75  $\mu\text{g}$  pmCherry-ESR1. These transfected cells were prepared for and imaged under similar conditions as the ER $\alpha$  foci formation assay, with the 561 laser line being used for imaging pDsRed2-SC35 and 461 laser being used to visualize pmTurquoise2-ESR1. Imaging was begun on stripped, live, MCF7 cells and was continued on the same live cells 30 after addition of 100 nM E<sub>2</sub>. After imaging, the FAST Airyscan images were again processed in the ZEN Black software package, but quantification of overlap was done by exporting the processed.czi from ZEN Black into Volocity software (Perkin Elmer, v.6.0.1). In Volocity, these image stacks were cropped to each cell and objects were identified using the identical 'Automatic' setting for each cropped image in both the red (SC35) and green (ER $\alpha$ ) channel. A representative single slice of a representative cell before and 30 min after 100 nM E<sub>2</sub> treatment was presented, as extended focus of all *z*-slices would fail to show the distinct patterning present on each slice. Distances between the centroid of each ER $\alpha$  foci object and the nearest SC35 object edge was calculated, as well as whether the ER $\alpha$  foci object had any overlap with any SC35 object. These 'nearest distance' measurements for all ER $\alpha$  foci in all cells were then pooled together and plotted as the proportion of all ER $\alpha$  foci objects at or below the listed distance. The overlap measurements were similarly pooled for all ER $\alpha$  foci in all cells.

### 1,6-hexanediol (1,6-HD) treatments with ER $\alpha$ foci.

MCF7 were transfected with pmTurquoise2-ESR1 and prepared for microscopy in identical conditions to those of the ER $\alpha$  foci formation Assay. MCF7 were pretreated with 100 nM E<sub>2</sub> for 16 h before imaging. Cells were then imaged before 1,6-HD treatment to establish a baseline. 1,6-HD was then added to cells at a final concentration of 5% in normal media, and images were again taken after 2 min of continuous treatment. A single representative and consistent slice of these image stacks were presented, as extended focus of all *z*-slices would fail to show the distinct ER $\alpha$  foci patterning on each slice.

### DNA FISH.

MCF7 cells were fixed with freshly made 4% paraformaldehyde in PBS for 8 min. Excess formaldehyde was quenched with 0.1 M Tris-HCl (pH 7.4) for 5 min. Coverslips were washed with PBS and stored at 4 °C until used. Before hybridization, coverslips were incubated in 0.1 N HCl for 5 min at room temperature and then washed twice with PBS.

Coverslips were incubated in PBS containing  $100 \mu\text{g ml}^{-1}$  RNAse A for 1 h at  $37^\circ\text{C}$ , followed by equilibration in 50% formamide/ $2\times$  SSC for 1 h. Then, 125 ng of probe in equal volume mixture of formamide and  $2\times$  hybridization buffer mix ( $4\times$  SSC/40% dextran sulfate) was used per coverslip. Coverslips on glass slides were heated for 6 min on a hotplate with temperature set at  $80^\circ\text{C}$  followed by overnight hybridization at  $37^\circ\text{C}$  in a humidified dark chamber. The coverslips were then washed twice with pre-warmed buffer containing 50% formamide/ $2\times$  SSC and twice with  $2\times$  SSC before being finally mounted with Vectashield antifade mounting medium with 4,6-diamidino-2-phenylindole (Vector Laboratories). For Immuno-DNA FISH, cells were incubated first with PBS containing 0.5% Triton X-100 and 5% BSA for 15 min at room temperature. Primary antibodies were used at a dilution of 1:50 in blocking buffer (0.1% Triton-100/5% BSA in PBS) for 1 h at  $37^\circ\text{C}$ , then washed three times in PBST (PBS containing 0.1% Triton X-100). Incubated with appropriated fluorescent conjugated secondary antibody (1:1,000) dilution for 30 min at room temperature. Cells were fixed for a second time with freshly prepared 2% paraformaldehyde for 10 min at room temperature followed by treatment with 0.1 M Tris-HCl (pH 7.4) for 5 min. They were then washed twice in PBS and DNA FISH protocol described above was resumed. All the probes used for the DNA FISH experiment are provided in Supplementary Table 5.

### RNA FISH.

Cells containing coverslips were fixed in 4% freshly prepared paraformaldehyde. They were washed twice with PBS with freshly added 2 mM ribonucleoside vanadyl complexes (Sigma-Aldrich). Cells were permeabilized and stored in 70% ethanol at  $4^\circ\text{C}$ . Before probe hybridization coverslips were incubated with wash buffer (10% formamide/ $2\times$  SSC) for 30 min at room temperature. RNA FISH probes were resuspended in hybridization buffer (10% formamide and 10% dextran sulfate in  $2\times$  SSC). Coverslips were incubated with probes overnight at  $37^\circ\text{C}$  in a humidification chamber. Post incubation washes were done using a pre-warmed wash buffer twice at  $37^\circ\text{C}$ . Immuno RNA FISH was performed using the protocol described above with addition of primary antibody mixed along with the RNA FISH probes and incubated overnight. Probes and primary antibody was washed off using wash buffer at  $37^\circ\text{C}$  followed by fluorescent conjugated secondary antibody incubation. Nuclei were counterstained by incubating in wash buffer containing Hoechst 33342 at a concentration of  $1 \mu\text{g ml}^{-1}$  for 15 min.

### DNA and RNA FISH probes.

All the BAC based probes for DNA FISH were purchased in the fluorescent labeled from Empire Genomics. Fosmids were obtained from CHORI. Fosmid based hybridization probes for DNA FISH were generated from  $1 \mu\text{g}$  fosmid using Nick Translation kit (Abbot Molecular), Green 496 or Orange 552 conjugate dUTP following manufacture recommended protocol. Then, 125 ng of each labeled probes,  $4 \mu\text{g}$  human Cot1 DNA (Thermo Fisher Scientific) and  $10 \mu\text{g}$  salmon testis DNA (Sigma-Aldrich) were used per coverslip. They were co-precipitated in ethanol and were resuspended in equal volume mixture of formamide and  $2\times$  hybridization buffer mix ( $4\times$  SSC/40% dextran sulfate) before the hybridization reaction. BAC and Fosmid clone IDs used in this study are in Supplementary Table 5.

RNA FISH probes were designed using Stellaris Probe Designer tool (Biosearch Technologies). Repeat masked intronic sequences of TFF1, NRIP1 and DOPEY2 were used as template for probe design. The entire mRNA sequence was used for generation of exonic probes. Probes were labeled with FAM, Quasar 570 or Quasar 670 dyes.

### **Microscopy for DNA and RNA FISH.**

Images were acquired using a Perkin Elmer Spinning Disk Confocal Microscope ( $\times 100$  Nikon Plane Achromatic oil immersion objective, numerical aperture: 1.40). The microscope was equipped with a Piezo-Z drive and EMCCD Hamamatsu 14-bit 1Kx1K camera. Z-stack data was acquired at a step size of 150 nm.

### **Image analysis.**

Three-dimensional image stacks were initially analyzed using Volocity software (Perkin Elmer, v.6.0.1). The functions 'Find Object' and 'Exclude Objects by Size' were combined for automatic detection of the FISH probe signals. For accurate and automated calculation of spatial distances between the probed loci, the three-dimensional coordinates and raw intensity sums (without background subtraction) of FISH probe signals were exported to CSV files using the Volocity software and were analyzed using custom software implemented with Python, NumPy and SciPy. To estimate the three-dimensional distance distribution between any two genomic loci, the centroids of the FISH signals from those loci were used to calculate a number (see below) of shortest distances for each nucleus and those distances were then pooled from all examined nuclei. This procedure assumed that each of the shortest distances obtained from each nucleus corresponded to loci located on the same chromosome. For experiments probing one diploid and one aneuploid locus, up to two shortest distances were obtained per nucleus. For experiments probing two aneuploid loci, the maximum number of shortest distances obtained per nucleus was equal to the smallest known copy number between the two loci in MCF7 cells. The median distances between control and test conditions were compared using the Wilcoxon rank sum test with continuity correction. The empirical cumulative distributions of distances were compared using the Kolmogorov-Smirnov test. To assess how the RNA FISH signal from a given locus varied with three-dimensional distance between that locus and a second locus, the raw intensity sums measured by Volocity software at the first locus were separated into two groups corresponding to distances ranging from 0 to 2  $\mu\text{m}$  and from 2 to 8  $\mu\text{m}$ . The median distances of the two groups were then compared using the Wilcoxon rank sum test with continuity correction. For calculation of median distances between RNA FISH foci and ER $\alpha$  cluster or ICG (SON antibody signal), distances calculated by Volocity, between edges of the closest of each signal, were used. Custom software used for this study is available on request.

### **Supplementary Material**

Refer to Web version on PubMed Central for supplementary material.

## Acknowledgements

The authors are grateful to J. Hightower for assistance with figure preparation. S.J.N. was a recipient of postdoctoral fellowship from American Heart Association (14POST19860025) and a T32 Fellowship (5T32DK007044). D.M. was supported by NIH-NIDDK Grant no. 5F32DK112682. Q.M. was a recipient of an American Cancer Society postdoctoral fellowship (PF-16-11-01-TBE). The authors gratefully acknowledge UB North Campus Confocal Imaging Facility (supported by NSF major research instrumentation Grant DBI no. 0923133) and A. Siegel for assistance with microscopy. Grant no. NS047101 supports the UCSD microscopy core facility. This work was supported by grants from the University at Buffalo, SUNY, College of Arts and Sciences to P.R.B. and to M.G.R. (nos. DK018477, DK039949, NS034934 and CA173903). M.G.R. is an investigator with the Howard Hughes Medical Institute.

## References

1. Bulger M & Groudine M Functional and mechanistic diversity of distal transcription enhancers. *Cell* 144, 327–339 (2011). [PubMed: 21295696]
2. Long HK, Prescott SL & Wysocka J Ever-changing landscapes: transcriptional enhancers in development and evolution. *Cell* 167, 1170–1187 (2016). [PubMed: 27863239]
3. Loven J et al. Selective inhibition of tumor oncogenes by disruption of super-enhancers. *Cell* 153, 320–334 (2013). [PubMed: 23582323]
4. Whyte WA et al. Master transcription factors and mediator establish super-enhancers at key cell identity genes. *Cell* 153, 307–319 (2013). [PubMed: 23582322]
5. Parker SC et al. Chromatin stretch enhancer states drive cell-specific gene regulation and harbor human disease risk variants. *Proc. Natl Acad. Sci. USA* 110, 17921–17926 (2013). [PubMed: 24127591]
6. Ji X et al. 3D chromosome regulatory landscape of human pluripotent cells. *Cell. Stem. Cell.* 18, 262–275 (2016). [PubMed: 26686465]
7. Kieffer-Kwon KR et al. Interactome maps of mouse gene regulatory domains reveal basic principles of transcriptional regulation. *Cell* 155, 1507–1520 (2013). [PubMed: 24360274]
8. Shin HY et al. Hierarchy within the mammary STAT5-driven Wap super-enhancer. *Nat. Genet.* 48, 904–911 (2016). [PubMed: 27376239]
9. Hnisz D, Shrinivas K, Young RA, Chakraborty AK & Sharp PA A phase separation model for transcriptional control. *Cell* 169, 13–23 (2017). [PubMed: 28340338]
10. Harlen KM & Churchman LS The code and beyond: transcription regulation by the RNA polymerase II carboxy-terminal domain. *Nat. Rev. Mol. Cell Biol.* 18, 263–273 (2017). [PubMed: 28248323]
11. Alberti S Phase separation in biology. *Curr. Biol.* 27, R1097–R1102 (2017). [PubMed: 29065286]
12. Banani SF, Lee HO, Hyman AA & Rosen MK Biomolecular condensates: organizers of cellular biochemistry. *Nat. Rev. Mol. Cell Biol.* 18, 285–298 (2017). [PubMed: 28225081]
13. Sin Y & Brangwynne CP Liquid phase condensation in cell physiology and disease. *Science* 357, eaaf4382 (2017).
14. Cho WK et al. Mediator and RNA polymerase II clusters associate in transcription-dependent condensates. *Science* 361, 412–415 (2018). [PubMed: 29930094]
15. Sabari BR et al. Coactivator condensation at super-enhancers links phase separation and gene control. *Science* 361, 10.1126/science.aar3958 (2018).
16. Boija A et al. Transcription factors activate genes through the phase-separation capacity of their activation domains. *Cell* 175, 1842–1855 (2018). [PubMed: 30449618]
17. Boehning M et al. RNA polymerase II clustering through carboxy-terminal domain phase separation. *Nat. Struct. Mol. Biol.* 25, 833–840 (2018). [PubMed: 30127355]
18. Chong S et al. Imaging dynamic and selective low-complexity domain interactions that control gene transcription. *Science* 361, eaar2555 (2018).
19. Kwon I et al. Phosphorylation-regulated binding of RNA polymerase II to fibrous polymers of low-complexity domains. *Cell* 155, 1049–1060 (2013). [PubMed: 24267890]

20. Lu H et al. Phase-separation mechanism for C-terminal hyperphosphorylation of RNA polymerase II. *Nature* 558, 318–323 (2018). [PubMed: 29849146]
21. Boulay G et al. Cancer-specific retargeting of BAF complexes by a prion-like domain. *Cell* 171, 163–178 (2017). [PubMed: 28844694]
22. Carroll JS et al. Chromosome-wide mapping of estrogen receptor binding reveals long-range regulation requiring the forkhead protein FoxA1. *Cell* 122, 33–43 (2005). [PubMed: 16009131]
23. Li W et al. Functional roles of enhancer RNAs for oestrogen-dependent transcriptional activation. *Nature* 498, 516–520 (2013). [PubMed: 23728302]
24. Hah N et al. A rapid, extensive, and transient transcriptional response to estrogen signaling in breast cancer cells. *Cell* 145, 622–634 (2011). [PubMed: 21549415]
25. Liu Z et al. Enhancer activation requires trans-recruitment of a mega transcription factor complex. *Cell* 159, 358–373 (2014). [PubMed: 25303530]
26. Pnueli L, Rudnizky S, Yosefzon Y & Melamed P RNA transcribed from a distal enhancer is required for activating the chromatin at the promoter of the gonadotropin  $\alpha$ -subunit gene. *Proc. Natl Acad. Sci. USA* 112, 4369–4374 (2015). [PubMed: 25810254]
27. Kim TK et al. Widespread transcription at neuronal activity-regulated enhancers. *Nature* 465, 182–187 (2010). [PubMed: 20393465]
28. Li W, Notani D & Rosenfeld MG Enhancers as non-coding RNA transcription units: recent insights and future perspectives. *Nat. Rev. Genet.* 17, 207–223 (2016). [PubMed: 26948815]
29. Dyson HJ & Wright PE Intrinsically unstructured proteins and their functions. *Nat. Rev. Mol. Cell Biol.* 6, 197 (2005). [PubMed: 15738986]
30. Tantos A, Han KH & Tompa P Intrinsic disorder in cell signaling and gene transcription. *Mol. Cell. Endocrinol.* 348, 457–465 (2012). [PubMed: 21782886]
31. Li W et al. Condensin I and II complexes license full estrogen receptor  $\alpha$ -dependent enhancer activation. *Mol. Cell* 59, 188–202 (2015). [PubMed: 26166704]
32. Bojcsuk D, Nagy G & Balint BL Inducible super-enhancers are organized based on canonical signal-specific transcription factor binding elements. *Nucleic Acids Res* 45, 3693–3706 (2016).
33. Kato M et al. Cell-free formation of RNA granules: low complexity sequence domains form dynamic fibers within hydrogels. *Cell* 149, 753–767 (2012). [PubMed: 22579281]
34. Mitrea DM et al. Methods for physical characterization of phase-separated bodies and membraneless organelles. *J. Mol. Biol.* 430, 4773–4805 (2018). [PubMed: 30017918]
35. Banerjee PR, Milin AN, Moosa MM, Onuchic PL & Deniz AA Reentrant phase transition drives dynamic substructure formation in ribonucleoprotein droplets. *Angew. Chem. Int. Ed. Engl.* 56, 11354–11359 (2017). [PubMed: 28556382]
36. Elbaum-Garfinkle S et al. The disordered P granule protein LAF-1 drives phase separation into droplets with tunable viscosity and dynamics. *Proc. Natl Acad. Sci. USA* 112, 7189–7194 (2015). [PubMed: 26015579]
37. Wang J et al. A molecular grammar governing the driving forces for phase separation of prion-like RNA binding proteins. *Cell* 174, 688–699 (2018). [PubMed: 29961577]
38. Shin Y et al. Spatiotemporal control of intracellular phase transitions using light-activated optodroplets. *Cell* 168, 159–171 (2017). [PubMed: 28041848]
39. Nott TJ et al. Phase transition of a disordered nuage protein generates environmentally responsive membraneless organelles. *Mol. Cell* 57, 936–947 (2015). [PubMed: 25747659]
40. Lin Y et al. Toxic PR poly-dipeptides encoded by the C9orf72 repeat expansion target LC domain polymers. *Cell* 167, 789–802 (2016). [PubMed: 27768897]
41. Kato M & McKnight SL A solid-state conceptualization of information transfer from gene to message to protein. *Annu. Rev. Biochem.* 87, 351–390 (2017). [PubMed: 29195049]
42. Franco HL, Nagari A & Kraus WL TNF $\alpha$  signaling exposes latent estrogen receptor binding sites to alter the breast cancer cell transcriptome. *Mol. Cell* 58, 21–34 (2015). [PubMed: 25752574]
43. Kaikkonen MU et al. Remodeling of the enhancer landscape during macrophage activation is coupled to enhancer transcription. *Mol. Cell* 51, 310–325 (2013). [PubMed: 23932714]



44. Brangwynne CP, Mitchison TJ & Hyman AA Active liquid-like behavior of nucleoli determines their size and shape in *Xenopus laevis* oocytes. *Proc. Natl Acad. Sci. USA* 108, 4334–4339 (2011). [PubMed: 21368180]
45. Shin Y et al. Liquid nuclear condensates mechanically sense and restructure the genome. *Cell* 175, 1481–1491 (2018). [PubMed: 30500535]
46. Brown JM et al. Association between active genes occurs at nuclear speckles and is modulated by chromatin environment. *J. Cell. Biol.* 182, 1083–1097 (2008). [PubMed: 18809724]
47. Shopland LS, Johnson CV, Byron M, McNeil J & Lawrence JB Clustering of multiple specific genes and gene-rich R-bands around SC-35 domains: evidence for local euchromatic neighborhoods. *J. Cell. Biol.* 162, 981–990 (2003). [PubMed: 12975345]
48. Skowronska-Krawczyk D et al. Required enhancer-matrin-3 network interactions for a homeodomain transcription program. *Nature* 514, 257–261 (2014). [PubMed: 25119036]
49. Quinodoz SA Higher-order inter-chromosomal hubs shape 3D genome organization in the nucleus. *Cell* 174, 744–757 (2018). [PubMed: 29887377]
50. Marzahn MR et al. Higher-order oligomerization promotes localization of SPOP to liquid nuclear speckles. *EMBO J.* 35, 1254–1275 (2016). [PubMed: 27220849]
51. Mitrea DM & Kriwacki RW Phase separation in biology; functional organization of a higher order. *Cell. Commun. Signal.* 14, 1 (2016). [PubMed: 26727894]
52. Ji X et al. SR proteins collaborate with 7SK and promoter-associated nascent RNA to release paused polymerase. *Cell* 153, 855–868 (2013). [PubMed: 23663783]
53. Pandit S et al. Genome-wide analysis reveals SR protein cooperation and competition in regulated splicing. *Mol. Cell* 50, 223–235 (2013). [PubMed: 23562324]
54. Lai F & Shiekhattar R Enhancer RNAs: the new molecules of transcription. *Curr. Opin. Genet. Dev.* 25, 38–42 (2014). [PubMed: 24480293]
55. Hah N, Murakami S, Nagari A, Danko CG & Kraus WL Enhancer transcripts mark active estrogen receptor binding sites. *Genome Res.* 23, 1210–1223 (2013). [PubMed: 23636943]
56. Mittag T & Parker R Multiple modes of protein-protein interactions promote RNP granule assembly. *J. Mol. Biol.* 430, 4636–4649 (2018). [PubMed: 30099026]
57. Keenholz RA et al. Oligomerization and ATP stimulate condensin-mediated DNA compaction. *Sci. Rep.* 7, 14279 (2017). [PubMed: 29079757]
58. Hirano T Capturing condensin in chromosomes. *Nat. Genet.* 49, 119–1420 (2017). [PubMed: 27918537]
59. D'Ambrosio C et al. Identification of cis-acting sites for condensin loading onto budding yeast chromosomes. *Genes Dev.* 22, 2215–2227 (2008). [PubMed: 18708580]
60. Haeusler RA, Pratt-Hyatt M, Good PD, Gipson TA & Engelke DR Clustering of yeast tRNA genes is mediated by specific association of condensin with tRNA gene transcription complexes. *Genes Dev.* 22, 2204–2214 (2008). [PubMed: 18708579]
61. Wood AJ, Severson AF & Meyer BJ Condensin and cohesin complexity: the expanding repertoire of functions. *Nat. Rev. Genet.* 11, 391–404 (2010). [PubMed: 20442714]
62. Crane E et al. Condensin-driven remodelling of X chromosome topology during dosage compensation. *Nature* 523, 240–244 (2015). [PubMed: 26030525]
63. Lin Y, Protter DS, Rosen MK & Parker R Formation and maturation of phase-separated liquid droplets by RNA-binding proteins. *Mol. Cell* 60, 208–219 (2015). [PubMed: 26412307]
64. Patel A et al. A liquid-to-solid phase transition of the ALS protein FUS accelerated by disease mutation. *Cell* 162, 1066–1077 (2015). [PubMed: 26317470]
65. Molliex A et al. Phase separation by low complexity domains promotes stress granule assembly and drives pathological fibrillization. *Cell* 163, 123–133 (2015). [PubMed: 26406374]

## References

66. Phair RD, Gorski SA & Misteli T Measurement of dynamic protein binding to chromatin in vivo, using photobleaching microscopy. *Methods Enzymol.* 375, 393–414 (2004). [PubMed: 14870680]



67. Schindelin J et al. Fiji: an open-source platform for biological-image analysis. *Nat. Methods* 9, 676–682 (2012). [PubMed: 22743772]

Author Manuscript

Author Manuscript

Author Manuscript

Author Manuscript

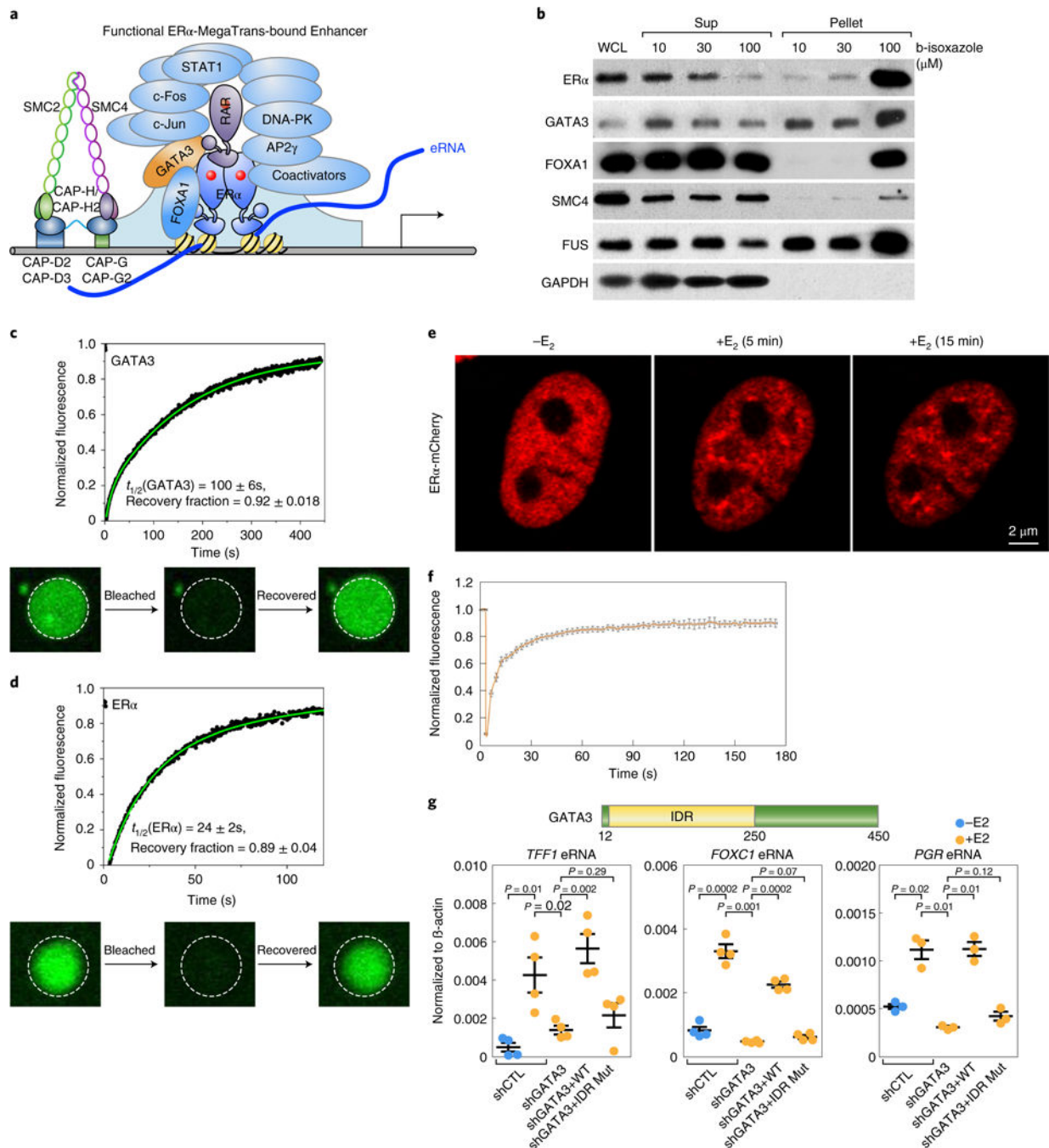


**Fig. 1 | Acutely active E<sub>2</sub>-responsive MegaTrans enhancers concentrate a protein complex that can undergo phase transition.**

**a**, Schematic representation of the ER $\alpha$ /MegaTrans complex recruited to E<sub>2</sub>-activated enhancers, which transcribe eRNAs and recruit the condensin I/II complexes. **b**, Western blot analyses showing that ER $\alpha$ , several MegaTrans components and condensin component SMC4 are precipitated by biotinylated isoxazole (b-isoxazole). FUS and GAPDH proteins are used as a positive and negative control for the assay, respectively. WCL, whole-cell lysate. **c,d**, FRAP data on phase-separated droplet formed in vitro by purified recombinant

GATA3-maltose binding protein (MBP) (c) and ER $\alpha$ -MBP (d). Top, charts show individual data points represented by dots, lines represent fitting to an exponential model to estimate the half-time of recovery. Bottom, representative images of in vitro droplets before and after photobleaching. e, Fluorescence microscopy images of a representative nucleus from MCF7 cells transfected with ER $\alpha$ -mCherry, before ( $-E_2$ ) or after ( $+E_2$ , 5 or 15min)  $E_2$  treatment. Scale bar, 2  $\mu$ m. f, Mean intensity and photobleaching normalized fluorescence of ER $\alpha$ -mTurquoise foci in  $E_2$  treated MCF7 cells relative to pre-bleaching signal. Error bars represent s.e.m. of  $n = 10$  cells per time point. g, Levels of eRNA from indicated enhancers, measured by reverse transcription PCR, from MCF7 cells depleted of endogenous GATA3 and expressing either wild type or IDR-deleted GATA3 (GATA3-IDR mut), after 1 h  $E_2$  stimulation. shCTL indicates non-targeting control shRNA. The IDR (aa 2–250) is shown in the schematics on top. Results are shown as individual data points (circles), mean $\pm$ s.d. (lines).  $P$  values were calculated with an unpaired Student's  $t$ -test. Data are representative of three independent experiments.

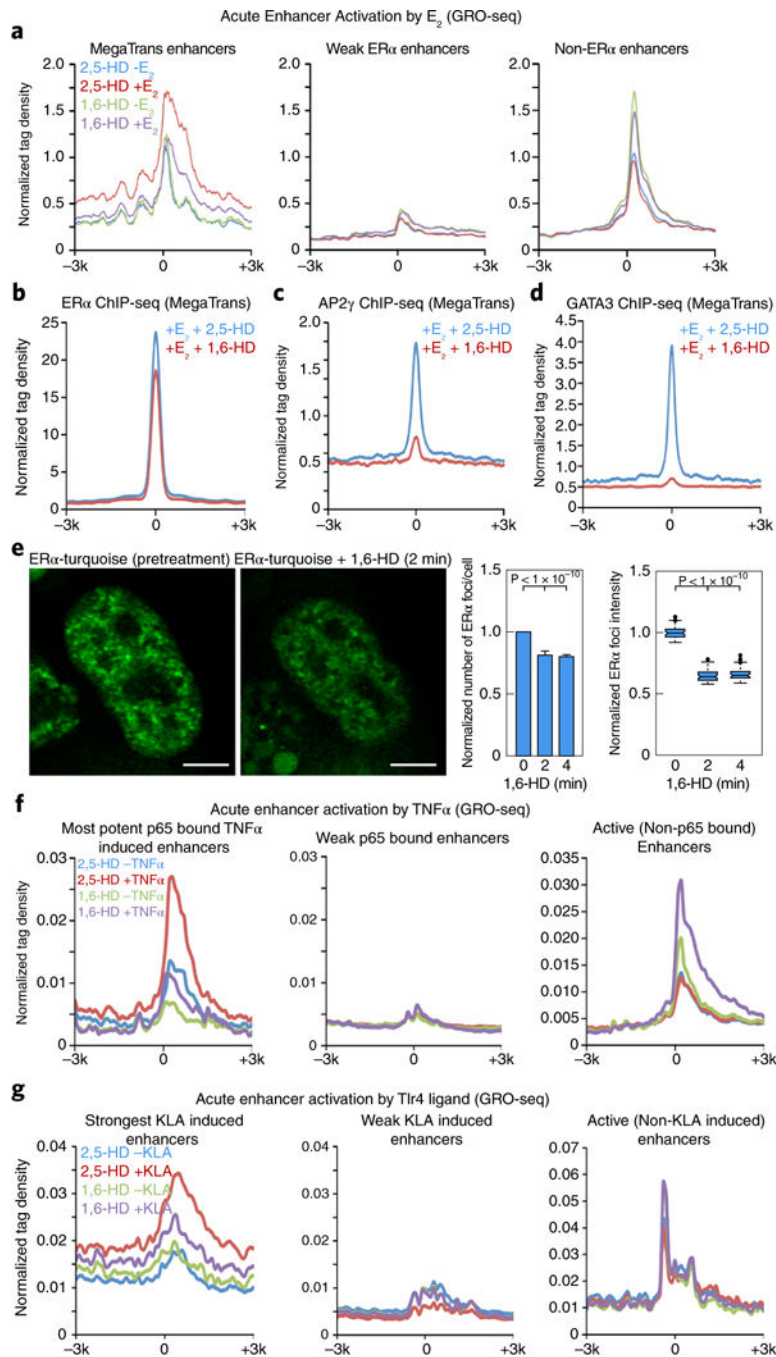


**Fig. 2 | Effect of phase-separation inhibition on acute enhancer transcriptional activation.**  
**a**, Meta-analysis of genome-wide GRO-seq data for enhancer activity in cells treated with 2,5-HD or 1,6-HD and  $E_2$ . Enhancers are classified as MegaTrans, weak ER $\alpha$  and non-ER $\alpha$ -bound enhancers. **b-d**, Meta-analysis of chromatin immunoprecipitation-(ChIP)-seq data representing the effect of 1,6-HD on chromatin recruitment of ER $\alpha$  (**b**), AP2 $\gamma$  (**c**) and GATA3 (**d**) on MegaTrans enhancers. **e**, Left, representative fluorescence microscopy images from MCF7 cells expressing ER $\alpha$ -Turquoise, showing loss of  $E_2$ -induced ER $\alpha$  foci on 1,6-HD treatment. Scale bars, 5 $\mu$ m. Right, quantification of foci number and intensity on

1,6-HD treatment. Foci number data are shown in bar graphs, as mean and s.e.m. of  $n = 3$  cells. Foci intensity data are shown as box plots, in which boxes represent interquartile ranges (IQRs); the whisker represents points in lower and upper quartiles within 1.5 IQR from lower and upper edges of IQR. The data are for  $n = 539$ , 446 and 436 estrogen-receptor foci for pre-, post-2 min and post-4min 1,6-HD time points, respectively. *P* values calculated with a two-tailed *z*-test. **f**, Meta-analysis of GRO-seq data showing impact of 1,6-HD on TNF $\alpha$  (1 h) activation of p65-bound enhancers in MCF7 cells. **g**, Meta-analysis of GRO-seq data showing impact of 1,6-HD on KLA-stimulated (30 min) enhancers in RAW264.7 cells.

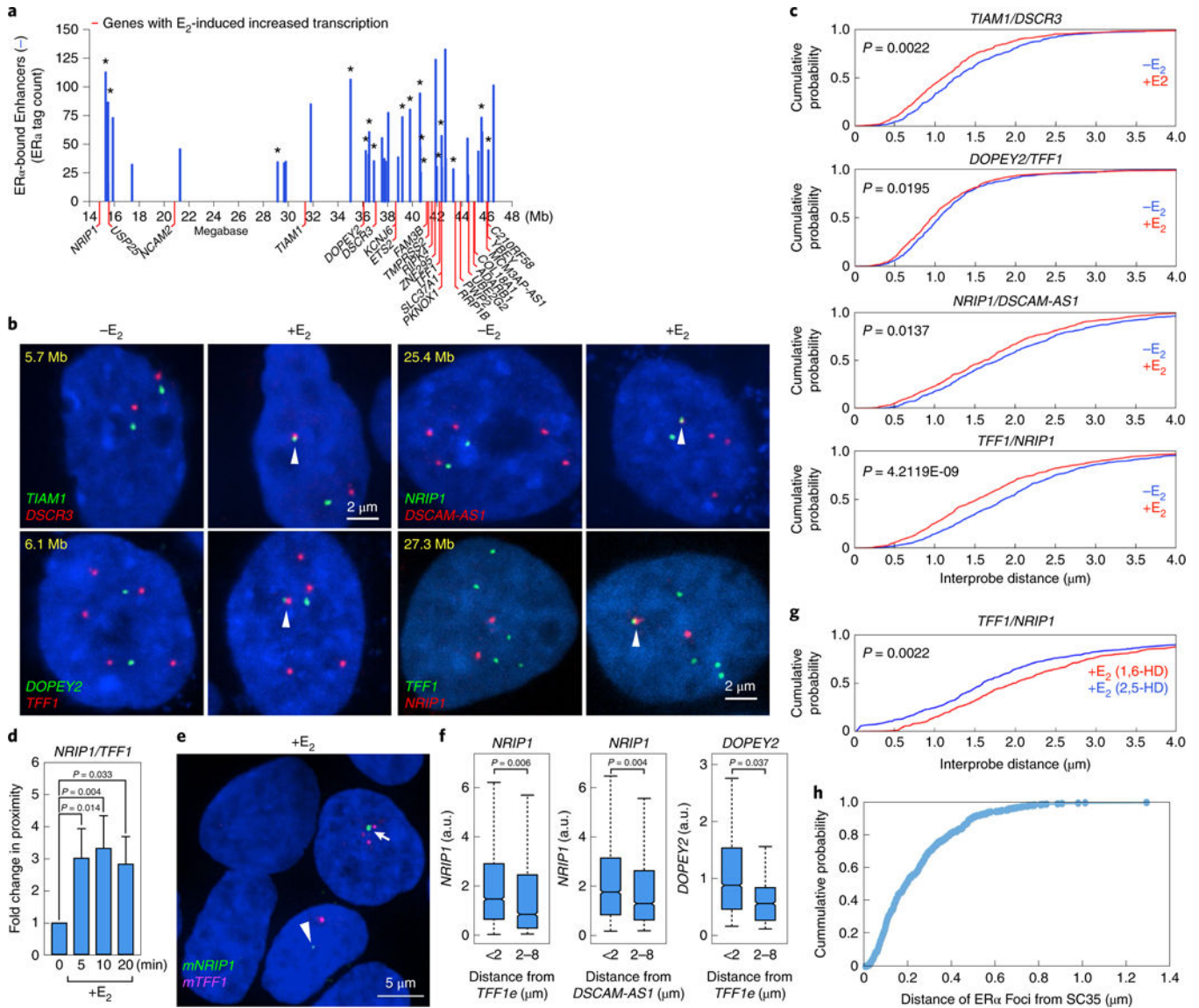


**Fig. 3 | Rapid ligand-induced interactions between distant MegaTrans enhancers.**  
**a**, Schematic diagram of human chromosome 21 showing enhancers with the highest levels of ER $\alpha$  binding and transcriptional activation in MCF7 cells following 1 h E $_2$  stimulation<sup>25,31</sup>. Active transcription units are listed below. \*, >1 enhancer. **b**, Representative DNA FISH images showing the E $_2$  induced proximity of indicated MegaTrans enhancer loci. Arrowhead points to the pair of loci in proximity. The *TFF1* and *DSCAM-AS1* loci are aneuploid in MCF7 cells, hence >2 FISH signals. Scale bars, 2  $\mu$ m. **c**, Cumulative distribution of distances between indicated MegaTrans enhancers, with and without E $_2$  stimulation. Data pooled from >200 nuclei from at least two independent experiments. *P* values were calculated using the Kolmogorov-Smirnov test. **d**, Time course quantifying the fold changes in fractions of *TFF1/NRIP1* allele pairs with spatial separation <600 nm. Error bars are theoretical standard deviations and *P* values were calculated using a bootstrap method (see Methods). For each time point, more than 650 distances were pooled from at least two independent experiments. **e**, RNA FISH using *NRIP1* and *TFF1* intronic



mRNA probes after 15min of E<sub>2</sub> treatment, showing increased transcription from *NRIP1* allele in proximity to *TFF1* (indicated by arrows) compared to a allele that is spatially distant from *TFF1* (indicated by arrowhead). **f**, Quantitation of RNA FISH signal intensity in relation to spatial distances between three different pairs of loci: *NRIP1* in relation to *TFF1* and to *DSCAM-AS1*; *DOPEY2* in relation to *TFF1*. a.u., arbitrary unit. Boxes represent IQRs; whiskers represent points in lower and upper quartiles within 1.5 IQR from lower and upper edges of IQR. For each pair of loci, at least 76 data points were pooled from two independent experiments. *P* values were calculated using a Wilcoxon rank sum test with continuity correction. **g**, Cumulative distribution of distances between *NRIP1* and *TFF1* enhancers in MCF7 cells after 50 min E<sub>2</sub> stimulation, treated with 2,5-HD or 1,6-HD. *P* values calculated using the Kolmogorov-Smirnov test. **h**, Cumulative frequency distribution of distances between E<sub>2</sub>-induced ER $\alpha$ -Turquoise foci and SC35-RFP (ICG marker).



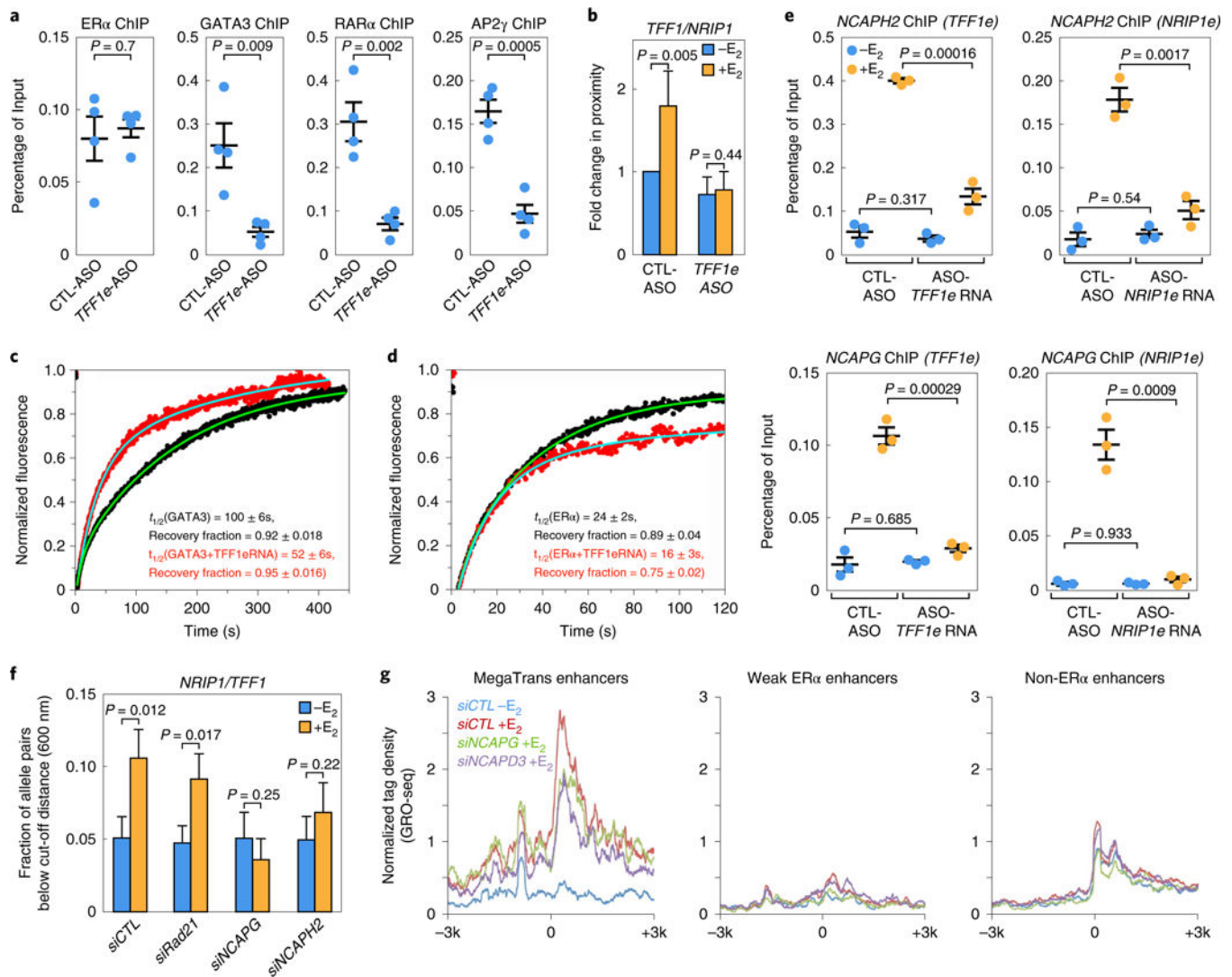


**Fig. 4 | Role of enhancer RNAs and condensins in E<sub>2</sub> induced chromosomal dynamics and eRNP assembly.**

**a**, ChIP data showing effect of *TFF1e* eRNA knockdown on recruitment of ER $\alpha$ , GATA3, RAR $\alpha$  and AP2 $\gamma$  to the *TFF1e* enhancer following E<sub>2</sub> treatment. CTL-ASO indicates non-targeting oligo used as control. Data shown as individual values (circles), mean and s.d. (lines).  $P$  values calculated with an unpaired Student's  $t$ -test. Data are representative of three independent experiments. **b**, Fold changes in fractions of *NRIP1/TFF1* allele pairs with separation below the cut-off distance, showing that *TFF1e* eRNA knockdown abolishes E<sub>2</sub> induced proximity between *TFF1* and *NRIP1* enhancer loci. Error bars show theoretical sample standard deviations and  $P$  values were calculated using a bootstrap method (see Methods). CTL-ASO indicates a non-targeting oligo used as a control. **c**, **d**, FRAP kinetics showing the effect of *TFF1* eRNA (0.20 mg/ml) on GATA3-MBP (**c**) or ER $\alpha$ -MBP or (**d**) fusion protein droplets in vitro. Data points are shown as circles, lines represent fitting to an exponential model to estimate the half-time or recovery. **e**, ChIP data showing effect of knocking down *TFF1* eRNA or *NRIP1e* eRNA on recruitment of condensin II subunit NCAPH2 (top) or condensin I subunit NCAPG (bottom) to the *TFF1e* and *NRIP1e* loci.

CTL-ASO indicates a non-targeting oligo used as a control. Data shown are individual values (circles), mean and s.d. (lines). *P* values were calculated with an unpaired Student's *t*-test. Data are representative of three independent experiments. **f**, Fractions of *NRIP1/TFF1* allele pairs with separation below the cut-off distance in cells with knockdown of the indicated proteins. Error bars indicate theoretical sample standard deviations and *P* values were calculated using a bootstrap method (see Methods). For each time point, more than 290 distances were pooled from at least two independent experiments. **g**, GRO-seq analyses showing effects of knockdown of *NCAPG* (condensin I) or *NCAPD3* (condensin II) on E<sub>2</sub>-activated enhancer transcription. siCTL represent scrambled oligos used as control; results are grouped for MegaTrans, weak ER $\alpha$  enhancers and non-ER $\alpha$ -bound enhancers.

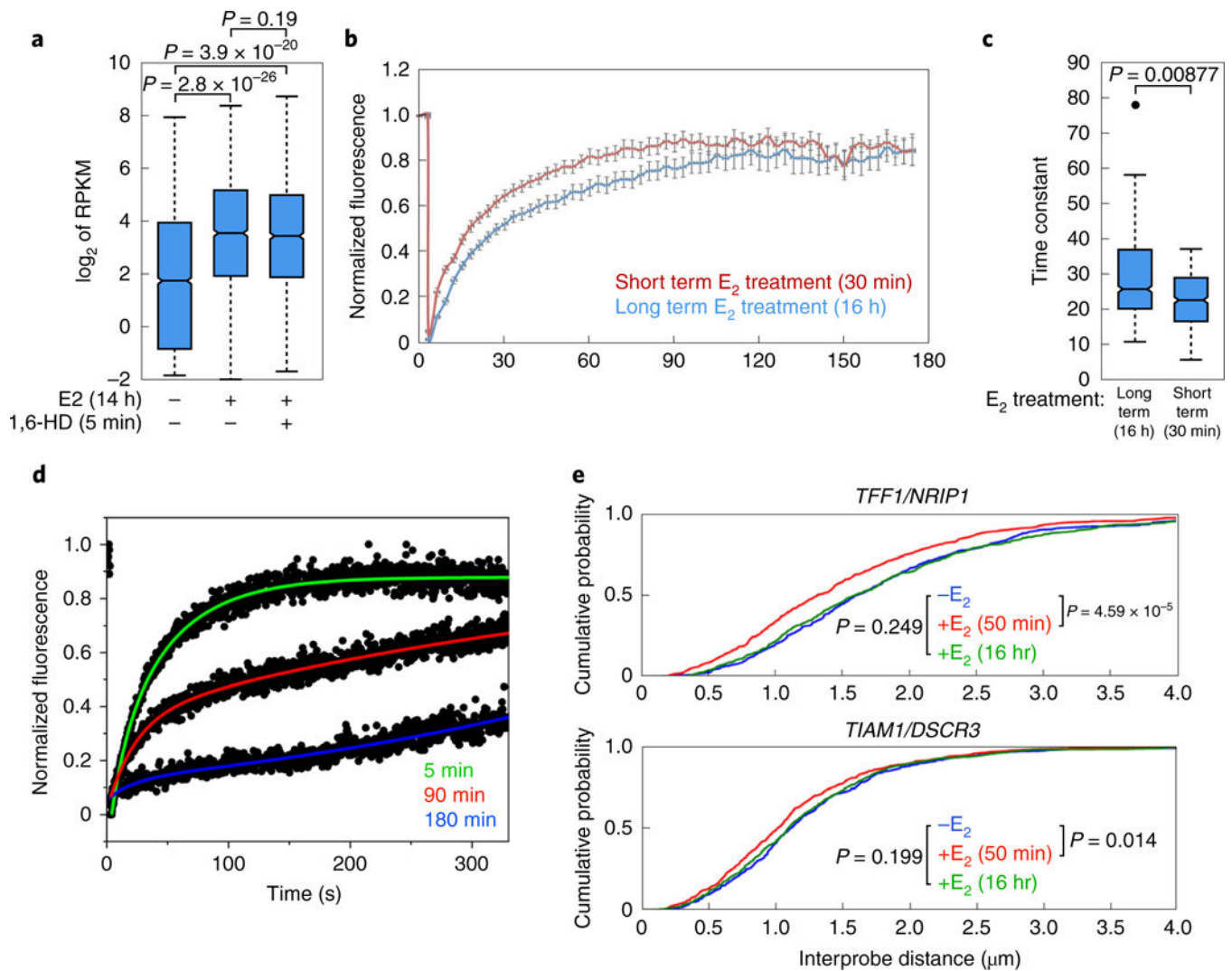


**Fig. 5 | Chronic stimulation with E<sub>2</sub> causes a fluid to hydrogel-like transition at enhancers and prevents ligand-induced enhancer proximity.**

**a**, Box plots of GRO-seq analysis MCF7 cells not stimulated with E<sub>2</sub> and not treated with 1,6-Hexanediol (1,6-HD) or E<sub>2</sub> stimulation for 14h with or without treatment with 1,6-HD for 5 min. Central line shows median; boxes represent the 25th and 75th percentiles; whiskers extend 1.5 times the interquartile range from the 25th and 75th percentiles.  $P$  values were calculated using two-tailed Student's  $t$ -test. **b**, Fluorescent recovery of ER $\alpha$ -mTurquoise foci in MCF7 cells after short-term (30 min) or long-term (16 h) E<sub>2</sub> treatment. Each point represents the mean intensity of the photobleaching normalized fluorescence relative to pre-bleaching signal. Error bars represent s.e.m. of  $n =$  at least 10 cells per time point. **c**, Box plots showing time constants of FRAP recovery of ER $\alpha$ -mTurquoise foci in MCF7 cells treated with E<sub>2</sub> for long term ( $n = 28$ ) and short term ( $n = 26$ ). Boxes represent IQRs; the whiskers represent points in lower and upper quartiles within 1.5 IQR from lower and upper edges of IQR.  $P$  values were calculated with a two-tailed  $z$ -test. **d**, FRAP analysis of in vitro droplets formed by a ternary mixture of GATA3-MBP (7 $\mu\text{M}$ ), ER $\alpha$ -MBP (7 $\mu\text{M}$ ) and TFF1 eRNA (0.20 mgml<sup>-1</sup>), and incubated for 5, 90 or 180 min. Data show a less rapid

fluorescence recovery with increasing time of incubation. Data points are represented by dots, lines represent fitting to an exponential model  $e$ , Cumulative distribution of distances between indicated MegaTrans enhancer pairs after short-term (50 min) and long-term (16 h)  $E_2$  treatment, demonstrating that the  $E_2$ -induced spatial proximity is lost on prolonged treatment. Data pooled from >150 nuclei examined in two independent experiments.  $P$  values were calculated using the Kolmogorov-Smirnov test.

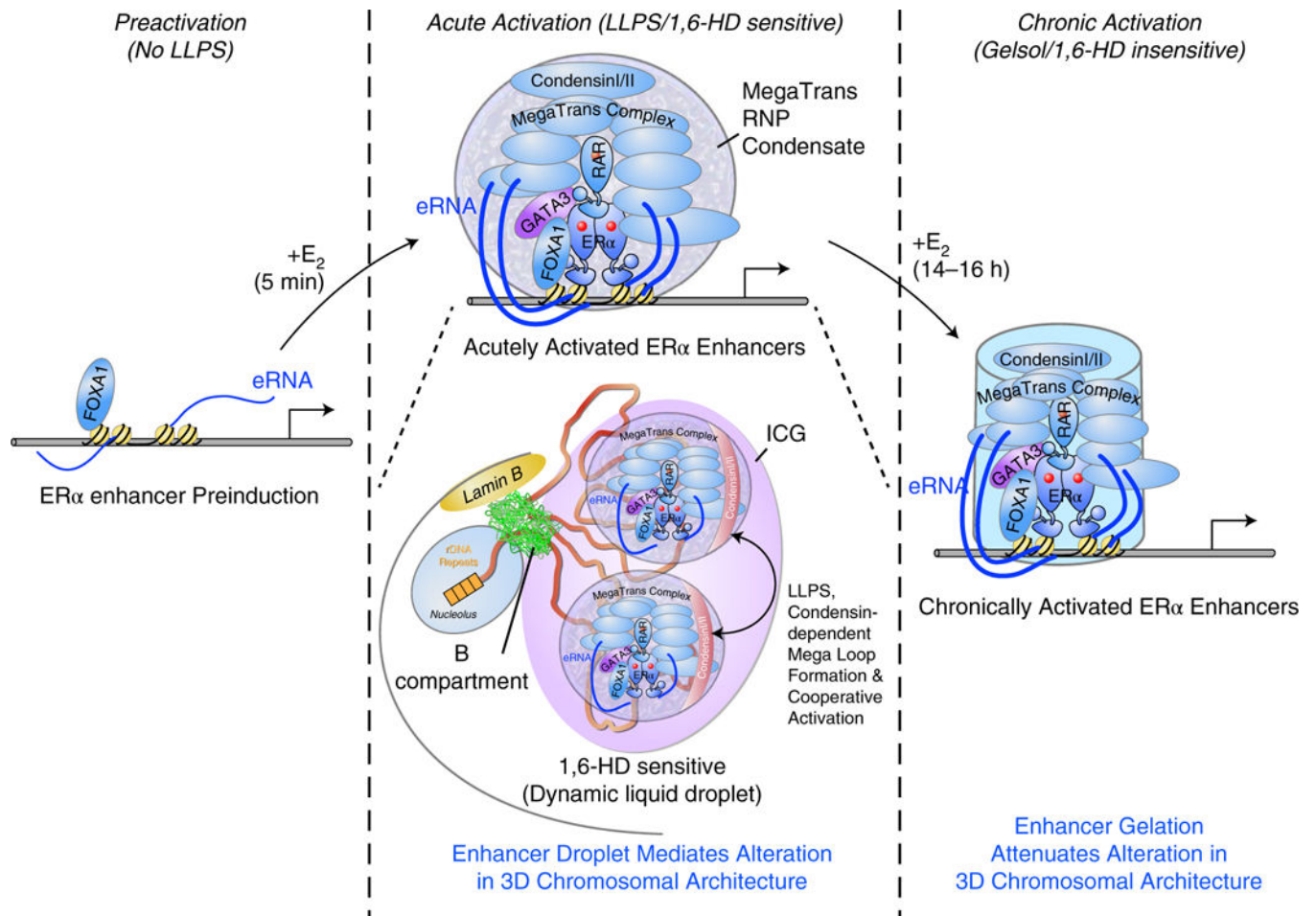


**Fig. 6 |. Model summary.**

MegaTrans enhancers are minimally active under unstimulated conditions. E<sub>2</sub> stimulation results in ERα dependent recruitment of MegaTrans complex, condensin complex and eRNA transcription, forming ‘megaloops’ between these enhancers. This results in an eRNA-dependent RNP (eRNP) assembled by phase separation. Chronic stimulation alters the physicochemical properties of this complex to a ‘gelsol state’ thus making them less sensitive to 1,6-HD. Maximal enhancer activation occurs with colocalization of the enhancer in the ICG, apparently resulting in increased concentration of transcriptional machinery and increased transcriptional robustness of component enhancers. Association with other nuclear structures such as the nucleolus and nuclear lamina represent a speculative model based on A/B compartments and rDNA locus in human chromosome 21.